A Fast and Dense Magneto-Optical Trap of Potassium Atoms Loaded From a Cold Buffer-Gas Beam

A THESIS PRESENTED
BY
MARYAM HIRADFAR
TO
THE DEPARTMENT OF PHYSICS

IN PARTIAL FULFILLMENT OF THE REQUIREMENTS
FOR THE DEGREE OF
BACHELOR OF ARTS
IN THE SUBJECT OF
CHEMISTRY AND PHYSICS
THESIS ADVISOR: PROFESSOR JOHN DOYLE
THESIS MENTORS: DR. ZACK LASNER AND DR. DEBAYAN MITRA

HARVARD UNIVERSITY
CAMBRIDGE, MASSACHUSETTS

MAY 2021

To my parents.

Acknowledgments

My time in the Doyle lab has been the most fulfilling aspect of my undergraduate experience, and I would like to thank the many people who made this experience possible, rewarding, and enjoyable for me.

I would like to thank my advisor, Professor John Doyle for his continuous support, guidance, and encouragement. His confidence in my capabilities as an undergraduate has made me continuously push the boundaries of what I think I am able to do, and to believe that anything is possible if we put our minds and hearts into it.

I would also like to thank my thesis mentors, Dr. Zack Lasner and Dr. Debayan Mitra for their invaluable dedication of time and energy to my education. I am deeply grateful for their patience with me as I have been navigating a research field previously unfamiliar to me, and their kind support all the way throughout.

I would like to thank Professor Lawrence Cheuk whose insight and support has been essential for this project. I would also like to thank him for his mentorship and for inspiring me to think outside the box, and to never be afraid of trying new solutions to problems. I would like to thank Ben Augenbraun for his guidance, kind mentorship, and his patience with the many mistakes I have made along the way and for teaching me how to positively

look at those mistakes as learning opportunities.

I would like to thank my friend and lab partner Eunice Lee with whom I spent countless hours working on this project. I owe a lot to Eunice, learning both from her academic knowledge and from her calm and kind character. Similarly, I would like to thank my friend and lab partner Sridhar Prabhu whose help and support was essential in the critical stages of assembling our experiment.

Additionally, I am thankful to all members of the Doyle lab for the wonderful community that has become my second family. I would like to give special thanks to the machine shop instructors and staff Stan Cotreau, Andy DiMambro, Steve Sansone, as well as the electronics shop instructor Jim MacArthur who have all taught me a lot and have always been there to answer my smallest and largest questions.

Scientific research is never complete without effective means to communicate and write about it. I would like to thank Professor Jenny Hoffman and Dr. Suzanne Smith for teaching me indispensable skills in effective scientific writing, and for giving me invaluable feedback on this thesis. I would also like to thank my wonderful friends Bobae Johnson and Alicia Zhang for reviewing chapters of my thesis.

None of these experiences would have been possible without the continuous support of my family. I am deeply grateful for my parents who have been my lifelong cheerleaders in scientific endeavors and who have made many sacrifices to provide me with the opportunity

to pursue my scientific interests in the United States.

Lastly, I would like to thank my best friend and roommate Austin Taylor who has been my day to day cheerleader. Without her words of encouragement, surprise chocolate cake deliveries and emotional support, the process of finishing this project and writing this thesis would have been unimaginably difficult.

Contents

0

Introduction

Atoms' simple and precisely controllable structures have made them ideal platforms for the experimental quest for new physics. In today's field of atomic, molecular, and optical (AMO) physics, samples of trapped ultracold atoms and molecules provide platforms for precision measurements, quantum simulations, and quantum chemistry experiments. In this thesis, I will discuss how we combined two methods of cooling, with the production of a cryogenic buffer gas beam (CBGB) to load a magneto-optical trap (MOT) of potassium atoms with loading rates much faster than, and densities comparable to, those achieved in traditional vapor-loaded atomic MOTs. The loading rate and density of a MOT are limiting factors for many experiments with short duty cycles. Improving these two factors will

potentially open new possibilities for what such experiments can achieve. The hybrid technique has been successfully used in the Doyle and other labs to create ultracold molecular traps for many years. However, it had never been used to create a trap of alkali atoms before. Our high density and rapidly loaded MOT of potassium atoms provides opportunities for future applications such as quantum simulations in optical tweezers and evaporative cooling for creating a Bose-Einstein condensate (BEC).

Historical Background

With the advent of lasers in the 60s [1], new possibilities for exploring the precise structure of atoms became possible. The optically coherent beams of a laser allow precise addressing of atomic transitions of a given frequency. Wineland, Drullinger and Walls were the first scientists to use this property of lasers to cool matter in 1978 [2]. Yes, you read that sentence correctly. They used *lasers* to *cool* matter! We tend to associate laser beams with powerful sources of energy that can burn holes in materials, destroy spaceships in movies, and in general, with heating things up. As a result, it sounds counter intuitive that lasers can cool matter down. It turns out that indeed, they can, if used in a specific manner, the key being that although lasers have high energy, they have low entropy. In some sense, the light from a laser is "ultracold." But how cold you might ask. While we are not able to reach absolute zero with laser cooling techniques alone, they do get us pretty close, typically to about a few hundred micro kelvins above absolute zero. But how cold is a few hundred micro kelvins above absolute zero? It might be helpful to think about the spectrum of naturally occurring temperatures. The coldest natural place in the universe, observed until 2017, is the Boomerang Nebula, which is a cloud in space with temperatures about 2K [3],

about the same temperature as the cosmic microwave background [4]. The core of the sun on the other hand is at about ten million kelvin. The temperatures achievable using laser cooling are therefore, about four orders of magnitude lower than the Boomerang Nebula, and about 11 orders of magnitude colder than the core of the sun. Although laser cooling by itself is unable to reach much lower temperatures, there are other techniques that, combined with laser cooling, could get us even colder. Reaching lower temperatures opens up the possibility of achieving a Bose-Einstein Condensate (BEC), which is a coherent state of matter with a large number of atoms in a single many-body ground state at the same time [5]. Achieving BEC is, of course, possible for bosonic species, since they can occupy the ground state simultaneously. In 1995 Eric Cornell and Carl Weiman used evaporative cooling along with laser cooling to reach temperatures of about 20 nK, and observed a BEC of rubidium atoms [6], and shortly after, Wolfgang Ketterle observed the very first BEC of sodium atoms [7]. Even though our experiment at this stage does not use techniques to go below the limit of a few hundred microkelvin, our dense and fast-loaded atomic trap provides a platform for BEC studies as a potential future direction.

Why Bother Cooling Atoms Down?

Thermal motion of atoms associated with high temperatures complicate many observations and experiments. At the simplest level, studying an object that is moving around with a fast speed is hard. At room temperature, the air molecules are moving at approximately 470 m/s which means that an air molecule will pass through a 1 cm region in about three hundredths of a millisecond. For comparison, a commercial airplane has a speed of about 200 m/s, and a blink of an eye lasts about a third of a second [8]. To observe an air molecule at

room temperature we need an instrument with a really good temporal resolution. Because of Heisenberg's uncertainty principle ($\Delta E \Delta t \geq \hbar$) having a really good temporal resolution will come at the cost of having really low energy resolution.

Additionally, the broader velocity distribution of hotter atoms causes the spectral lines to broaden, and hence, lower the resolution with which each spectral line can be resolved. Any ensemble of atoms or molecules at a certain temperature has a velocity distribution with a width proportional to the square root of absolute temperature. This means that the colder temperatures become, the likelihood of finding a particle with velocities very different from the average velocity becomes lower and lower. This is also important because due to the Doppler effect, atoms of different velocities absorb lights that have shifted frequencies compared to the transition frequency of an atom at rest. Consequently, atoms at higher temperatures have higher likelihoods of absorbing frequencies of light that are farther from the transition frequency at rest. This phenomenon is what we mean by "broadening of spectral lines." Hence, for increasing the precision of spectroscopy and measurements, it is necessary to go to lower temperatures at which quantum objects such as atoms and molecules can be interrogated for long times and spectral lines can be better resolved.

Current And Past Successes of cryogenic buffer gas beams (CBGB)

The Doyle lab pioneered the hybrid technique of using a cryogenic buffer gas beam (CBGB) to load a magneto-optical trap (MOT). To date, the technique has been used to trap atomic species of lanthanides Yb, Tm, Er, and Ho [9], as well as molecular species [10, 11, 12]. Recent experiments in our lab have used CBGBs to detect single molecules of CaF in optical tweezers [13], and demonstrate a 1D MOT of CaOH [10]. Additional experiments in the

Doyle lab have used CBGBs of YbOH [11] and $CaOCH_3$ [12] to cool these species below the Doppler limit. Our goal has been to extend the CBGB technique to alkalis which have much simpler structures compared to both lanthanides and molecules, and are therefore promising candidates for achieving higher loading rates and MOT densities.

Outline

- Chapter 1: I will describe the theory of laser cooling and trapping in detail in this chapter. The mathematical detail and rigor of this chapter assumes some knowledge of quantum mechanics, electromagnetism, and linear algebra. However, these details are by no means necessary for getting a general understanding of this thesis. The opening paragraphs in each section give some general description before getting into the details.
- Chapter 2: Discussion of Doppler-free modulation transfer spectroscopy, as well as saturated absorption spectroscopy.
- Chapter 3: This chapter is about the design and construction of the beam box, preparation of material, and various components.
- Chapter 4 Discussion of the experimental setup for the MOT optics, 1D transverse Doppler cooling, chirped slowing, and the experiment sequence.
- Chapter 5: MOT characterization and results.
- Chapter 6: Discussion of the significance of results as well as current and future improvements to the setup.

re

1

Theory of Laser Cooling and Trapping

In this chapter, we will present the theoretical background that is needed to understand the laser cooling and trapping techniques that we implement in our experiment. We will start by outlining the atomic structure and optical properties of ^{39}K and present an overview of Doppler cooling and magneto-optical trapping.

1.1 Potassium

1.1.1 General Background

Potassium (K) belongs to the category of alkali metal atoms, has an atomic number of 19, and has three naturally occurring isotopes: ^{39}K, ^{40}K, and ^{41}K. For our experiment, we use a natural sample of potassium as our atom source, and as a result, our source contains all three isotopes. Since our goal is to obtain a high number of atoms after ablation to laser cool, we tailor our experiment to laser cool ^{39}K, which is the most abundant potassium isotope. Table 1.1 presents a summary of the properties of ^{39}K, ^{40}K, and ^{41}K.

Isotope A	Neutrons N	Abundance (%)	$m(u)$	I	
39	20	93.2581	38.9637	3/2	bosonic
40	21	0.0117	39.9639	4	fermionic
41	22	6.7302	40.96182	3/2	bosonic

Table 1.1 : A summary of properties of the naturally occurring isotopes of potassium, with A being the mass number, m denoting the atomic mass, and I the nuclear spin. This table was taken from Tiecke's "properties of potassium." [16]

1.1.2 Optical Transitions of ^{39}K

Even in the absence of external fields, ^{39}K has a rich electronic structure that arises from both fine splitting and hyperfine splitting of the energy levels. A schematic of the electronic energy splittings for the three isotopes, for the valence level of potassium ($n = 4$), is presented in figure 1.1. We outline the theory of fine splitting and hyperfine splitting for ^{39}K below.

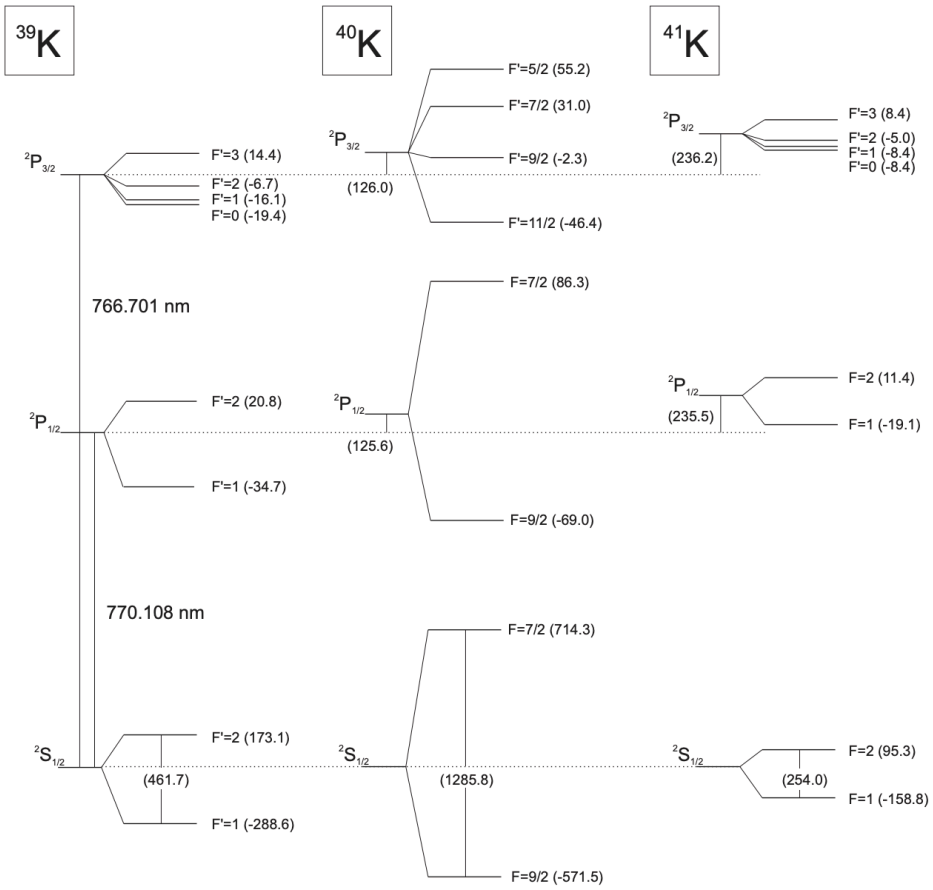

Figure 1.1: Schematic of the hyperfine energy levels of ^{39}K, ^{40}K, and ^{41}K for $n = 4$. Figure from Tiecke's document on properties of Potassium [16]

.

1.1.3 Fine Structure Splitting

The fine structure splitting arises from spin-orbit coupling with the Hamiltonian[14]

$$H_{\text{so}} = (g_s - 1)\frac{\hbar^2}{2m_e^2c^2}\left(\frac{1}{r}\frac{\partial V}{\partial r}\right)\mathbf{S}\cdot\mathbf{L}, \tag{1.1}$$

where $g_s \approx 2$ is the spin g-factor, V is the coulomb potential, **S** is the electron spin, and **L** is the electron orbital angular momentum.

In the presence of the spin-orbit interaction, the spin **S** and the orbital angular momentum **L** are no longer individually conserved. Instead, the total electronic angular momentum $\mathbf{J} = \mathbf{L} + \mathbf{S}$ is conserved. In other words, the Hamiltonian does not commute with the operators **L** and **S** and as a result, the eigenstates of these operators are not "good" quantum numbers. To find the "good" quantum numbers we define the total electronic angular momentum **J** such that [15]

$$\begin{aligned} \mathbf{J}^2 &= (\mathbf{L} + \mathbf{S}) \cdot (\mathbf{L} + \mathbf{S}) \\ &= L^2 + S^2 + 2(\mathbf{L} \cdot \mathbf{S}). \end{aligned} \tag{1.2}$$

Based on the above expression, the Hamiltonian does commute with $\mathbf{J}^2$, and consequently, with $\mathbf{L}^2$, and $\mathbf{S}^2$. The eigenvalues of these operators which are correspondingly $\hbar^2 j(j+1)$, $\hbar^2 l(l+1)$, and $\hbar^2 s(s+1)$ are "good" quantum numbers. A rearrangement of equation 1.1.3 determines the eigenvalues of the interaction term, $(\mathbf{L}.\mathbf{S})$[15]

$$\frac{\hbar^2}{2}[j(j+1) - l(l+1) - s(s+1)]. \tag{1.3}$$

The energy eigenvalues of the spin orbit Hamiltonian (equation 1.1) will be proportional to the above expression. We can see that, if $l \neq 0$, the degeneracy in l is lifted [19]. In the case of K, this means that the first excited state, 4^2P, which has $L = 1$, and $S = \frac{1}{2}$ gets split into two states, since $|L - S| \leq j \leq |L + S|$. As a result, we get $4^2P_{1/2}$ with $J = \frac{1}{2}$, and $4^2P_{3/2}$ with $J = \frac{3}{2}$ [14]. This fine structure splitting gives rise to the D_1, and the D_2 lines,

which correspond to the $4^2S_{1/2} \longrightarrow 4^2P_{1/2}$, and $4^2S_{1/2} \longrightarrow 4^2P_{3/2}$ transitions respectively [16].

1.1.4 Hyperfine Splitting

Since ^{39}K has a nuclear spin of $I = \frac{3}{2}$, the energy levels further split due to interaction between this nuclear spin and the total electronic angular momentum **J**. Similar to our discussion regarding fine structure splitting, when considering the nuclear spin, **I** and **J** are not individually conserved. Instead,the total angular momentum $\mathbf{F} = \mathbf{I} + \mathbf{J}$ is conserved.

To obtain the hyperfine Hamiltonian, we need to consider the coupling between **I** and **J**. The hyperfine Hamiltonian then, can be derived [14]

$$H_{\text{hfs}} = A_{\text{hfs}}\mathbf{I} \cdot \mathbf{J}. \tag{1.4}$$

Where A_{hfs} is the hyperfine structure constant. From this Hamiltonian, the hyperfine energy levels can be calculated as [14]

$$\frac{A_{\text{hfs}}}{2}\big[F(F+1) - I(I+1) - J(J+1)\big]. \tag{1.5}$$

So far, the energy level calculations relied on the assumption that the electron and the nucleus act as point charges. For atoms with more than one electron, however, calculating the energies at the hyperfine level requires that we go beyond the point charge assumption and include higher order terms [17]. The next level of precision would be to consider the electric quadrupole moment term [17]. Derivations and extensive discussion of the electric quadrupole term can be found in sources by Arimondo [18] and LeBlanc [17]. Here we

only note the result for the Hamiltonian [17],

$$H_{\text{quad}} = \frac{e^2 q_J Q}{2I(2I-1)J(2J-1)} \left[3(\mathbf{I}\cdot\mathbf{J})^2 + \frac{3}{2}(\mathbf{I}\cdot\mathbf{J} - \mathbf{I}^2\mathbf{J}^2) \right]. \tag{1.6}$$

Taking the electric quadrupole term into account, the full hyperfine Hamiltonian can be written as the sum of equation 1.4 and equation 1.6,

$$H_{\text{hfs}} = A_{\text{hfs}}\mathbf{I}\cdot\mathbf{J} + B_{\text{hfs}} \frac{3(\mathbf{I}\cdot\mathbf{J})^2 + \frac{3}{2}(\mathbf{I}\cdot\mathbf{J}) - \mathbf{I}^2\mathbf{J}^2}{2I(2I-1)J(2J-1)}. \tag{1.7}$$

Here, the constant $B_{\text{hfs}} = e^2 q_J Q$ is used and is experimentally measured for different atoms [17].

Consider the dot product term $\mathbf{I}\cdot\mathbf{J}$, which is given by [16]

$$\mathbf{I}\cdot\mathbf{J} = \frac{\left(\mathbf{F}^2 - \mathbf{I}^2 - \mathbf{J}^2\right)}{2}. \tag{1.8}$$

The hyperfine energy levels can be derived:

$$E_{\text{hfs}} = \frac{1}{2}A_{\text{hfs}}K + B_{\text{hfs}} \frac{\frac{3}{2}K(K+1) - 2I(I+1)J(J+1)}{2I(2I-1)2J(2J-1)}, \tag{1.9}$$

where K has the following form:

$$K = F(F+1) - I(I+1) - J(J+1).$$

Although the fine structure did not cause splitting of the ground state $4^2S_{1/2}$ since for the ground state we have $L = 0$, the above relation, indicates that the ground state has hyper-

fine splitting. For $4^2S_{1/2}$, we have $L = 0, S = \frac{1}{2}$, and consequently $J = \frac{1}{2}$. With $I = \frac{3}{2}$, and with the relation $|J - I| \leq F \leq |J + I|$, the ground state gets split into two levels with $F = 1$ and $F = 2$ [19].

1.2 Laser Cooling and Trapping

Our cooling and trapping of the K atoms rely on velocity-dependent and position-dependent forces. In order to slow the atoms down, we take advantage of Doppler cooling in an "optical molasses," which reduces the velocity of the atoms by giving them many momentum kicks in the opposite direction from their movement. Position-dependent trapping forces are provided by configuring a spatially varying magnetic field in combination with laser light, and by the consequent spatially varying Zeeman shift produced in the D_2 transition line (see figure 1.4). Both the optical molasses and the spatially varying Zeeman shift are combined in a magneto-optical trap (MOT), which produces cooling and trapping forces simultaneously.

In the upcoming subsections, I will first discuss the theory of Doppler cooling, followed by discussion of the Zeeman effect and the Magneto-Optical Trap.

1.2.1 Doppler Cooling

Imagine an incoming beam of atoms that we wish to slow down, and eventually trap in a confined space. One common, yet counter-intuitive way to do so, is to direct a laser beam at the incoming atoms. While in everyday life, we tend to associate lasers with heat and burning, we can take advantage of the extreme frequency coherence of lasers to address a specific transition in the atoms, and with the help of a few tricks, slow them down.

Each photon in the laser beam carries energy $E = \hbar\omega$, and momentum $\vec{p} = \hbar\vec{k}$. If the frequency of the photon matches the frequency of the target transition, the photon has a high likelihood of getting absorbed by the atom. In the process of absorption, two important events take place. One is that, by conservation of momentum, the photon transfers its momentum of $\hbar k$ to the atom, and the other is that it uses its energy of $\hbar\omega$ to kick an electron from the ground state of the transition to the excited state. The electron will decay back down, after some time, releasing a photon with frequency ω, by spontaneous emission. However, these spontaneous emission events take place randomly in all directions, and their effect on the momentum of the atoms mostly cancels out when averaged over many scattering events. The net effect is that only the momentum kick that is given to the atom in the opposite direction from its motion ends up mattering, and will slow the atom down. The velocity change in this event can be calculated using conservation of momentum,

$$v_{\text{recoil}} = \frac{\hbar k}{m}. \tag{1.10}$$

Ignoring the spontaneous emission events, the lower limit on the temperature that can be achieved by laser cooling an ensemble of atoms is then given by

$$T_{\text{recoil}} = \frac{\hbar^2 k^2}{m k_B}, \tag{1.11}$$

which corresponds to a change in energy of $\frac{1}{2}k_B T_{\text{recoil}}$. We can define the recoil frequency ω_{recoil} to be [20]

$$\omega_{\text{recoil}} = \frac{\hbar k^2}{2m}, \tag{1.12}$$

where k_B is the Boltzmann constant.

The total force that is applied to an atom due to absorption and spontaneous emission is referred to as the scattering force [20]. This force is given by the rate of change of momentum over time, and can be written as [21]

$$\vec{F}_{\text{scattering}} = R_{\text{scattering}} \hbar \vec{k}, \tag{1.13}$$

where $R_{\text{scattering}}$ is the scattering rate [21]. As derived in [22], it can be shown that the scattering force can be written as

$$F_{\text{scattering}} = \hbar k \frac{\Gamma}{2} \cdot \frac{I/I_{\text{sat}}}{1 + I/I_{\text{sat}} + (2\delta/\Gamma)^2}, \tag{1.14}$$

where Γ is the linewidth of the transition, I is the beam intensity, I_{sat} is the saturation intensity, and δ is the laser detuning [22].

So far, we have neglected the Doppler effect arising from the motion of atoms. In reality, since the atoms are moving, they will experience a Doppler detuning of $\delta_{\text{Doppler}} = -\vec{k} \cdot \vec{v}$. For instance, if we have a photon with frequency ω, and an atom that is moving toward this photon, we will have a positive δ_{Doppler} (note that $\vec{k} \cdot \vec{v}$ is negative in this case). As a result, the atom will "see" the frequency of the photon as blue-shifted. Assuming that the laser beam has a detuning of δ relative to the transition frequency, the total detuning is now given by [20]

$$\delta_{\text{total}} = \delta - k \cdot v.$$

Taking advantage of this effect, we can red-detune the laser beam so that we selectively address the atoms that are moving toward the laser beam with a higher probability.

Following the derivation in Naaman's thesis [22], we use the overall detuning in equation 1.2.1 to rewrite the expression for $F_{\text{scattering}}$ in equation 1.14 for moving atoms

$$F_{\text{scattering}} = \hbar k \frac{\Gamma}{2} \cdot \frac{I/I_{\text{sat}}}{1 + I/I_{\text{sat}} + (2\delta_{\text{total}}/\Gamma)^2} \cdot \tag{1.15}$$

This equation, however, considers the interaction of the atom with only one laser beam. To slow the atomic beam in both directions, we use a pair of counter-propagating beams. To calculate the overall force, we need to add in the contribution from this second laser beam [22],

$$F_{\text{scat,total}} = \hbar k \frac{\Gamma}{2} \left[\frac{I/I_{\text{sat}}}{1 + I/I_{\text{sat}} + (2\delta^{+}_{\text{total}}/\Gamma)^2} - \frac{I/I_{\text{sat}}}{1 + I/I_{\text{sat}} + (2\delta^{-}_{\text{total}}/\Gamma)^2} \right]. \tag{1.16}$$

Here, $\delta^{+}_{\text{total}}$ and $\delta^{-}_{\text{total}}$ represent the total detuning for the case of the atom's relative motion toward and away from the counter-propagating beams respectively. This relation is plotted in figure 1.2 for ^{39}K.

We can simplify this expression by approximating at $v \ll \frac{\delta}{k}$ [22]. The result is [22]

$$\begin{aligned} F_{scat,total} &\approx \frac{4\hbar k^2 (I/I_{\text{sat}})(2\delta/\Gamma)}{[1 + I/I_{\text{sat}} + (2\delta/\Gamma)^2]^2} v \\ &\equiv -\alpha v. \end{aligned} \tag{1.17}$$

From this expression, we can see that the counter-propagating pair of lasers imparts a velocity dependent scattering force on the atom. Additionally, this force acts in the opposite

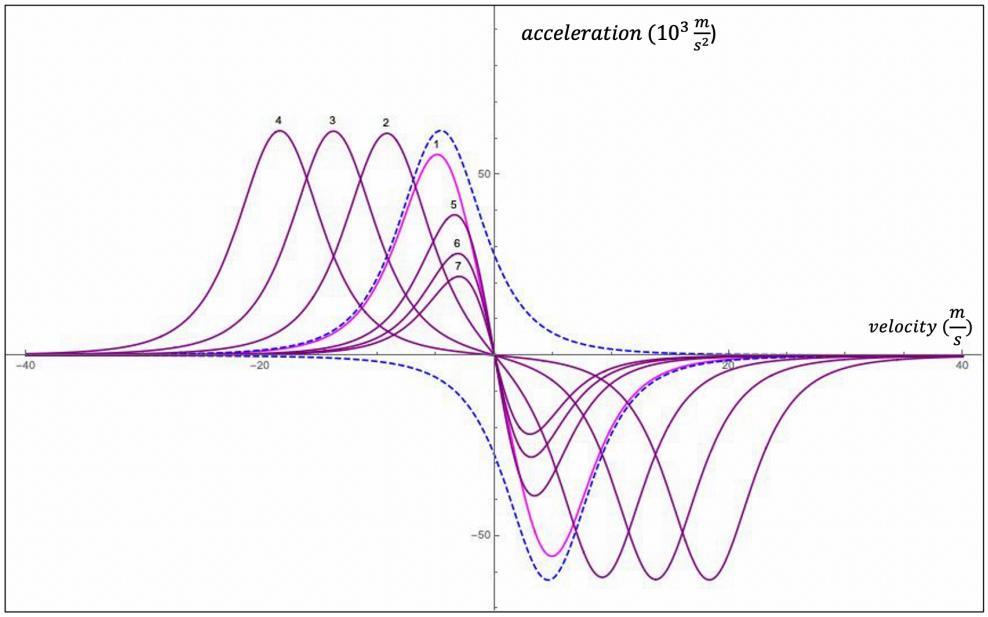

Figure 1.2: Acceleration of the ^{39}K plotted as a function of velocity, under the influence of two counter-propagating red-detuned beams, in a 1-D MOT from equation 1.16. Each labeled line is plotted for a specific value of detuning: 1:$\delta = -\Gamma$, 2:$\delta = -2\Gamma$, 3:$\delta = -3\Gamma$, 4:$\delta = -4\Gamma$, 5:$\delta = -0.5\Gamma$, 6:$\delta = -0.333\Gamma$, 7:$\delta = -0.250\Gamma$. The dashed lines represent the separate components of the force, arising from interaction with the left and right beams, in the case of $\delta = -\Gamma$. The ratio I/I_{sat} is taken to be 1 in all curves. It can be seen that for small speeds, the acceleration is linear to a good approximation, and as a result, the force on the atoms could be estimated as a velocity-dependent drag force [20], as outlined in equation 1.17.

direction of motion for $\delta < 0$ (red detuning of the laser light), and can be thought of as a drag force [22]. If we configure our beams in three counterpropagating pairs, we can employ this damping force from all directions. This setup is referred to as "optical molasses" [23].

1.2.2 Doppler Limit

Although the random spontaneous emissions do not cause a net velocity change over many scattering events, since $\langle \vec{v} \rangle = 0$ by symmetry, $\langle v^2 \rangle > 0$, and as a result, the kinetic energy

will increase. We can therefore, look at the steady state situation where the rate of heating from the random scattering events equals the Doppler cooling rate. Referring back to equation 1.17 we can write down the cooling rate $R_{\text{cooling}} = F_{\text{scat,total}}\, v$ as

$$R_{\text{cooling}} = F_{\text{scat,total}}\, v^2 = -\frac{2\alpha}{m} E_{\text{kinetic}}. \tag{1.18}$$

The heating rate is given by the average rate of change in energy of the atoms for the random scattering events

$$R_{\text{heating}} = 2\frac{\hbar^2 k^2}{2m} R_{\text{scattering}}. \tag{1.19}$$

Here, $\frac{\hbar^2 k^2}{2m}$ is the average change in the kinetic energy of the atoms for every scattering event, and the factor of two accounts for the fact that we have two counter-propagating beams of light [22]. To explore the steady state, we set these two rates equal to each other

$$\begin{aligned} R_{\text{cooling}} &= R_{\text{heating}} \\ \frac{2\alpha E_{\text{kinetic}}}{m} &= \frac{\hbar^2 k^2 R_{\text{scattering}}}{m}. \end{aligned}$$

Solving for energy, we get that

$$E_{\text{kinetic}} = \frac{\hbar^2 k^2 R_{\text{scattering}}}{2\alpha}. \tag{1.20}$$

For small velocities where $v \ll \delta/k$, we can write the scattering rate as

$$R_{\text{scattering}} = \frac{\Gamma}{2} \cdot \frac{I/I_{\text{sat}}}{1 + I/I_{\text{sat}} + (2\delta/\Gamma)^2}. \tag{1.21}$$

Using equation 1.20, substituting for α based on equation 1.17, and substituting for $R_{\text{scattering}}$ from equation 1.21 we get the steady state energy

$$E_{\text{kinetic}} = -\frac{\hbar^2\Gamma^2}{16\delta}\left(1 + I/I_{\text{sat}} + \frac{4\delta^2}{\Gamma^2}\right).$$

Assuming that $I \ll I_{\text{sat}}$, we can simplify the above equation to

$$E_{\text{kinetic}} = -\frac{\hbar^2\Gamma^2}{16\delta}\left(1 + \frac{4\delta^2}{\Gamma^2}\right).$$

Setting the energy equal to $\frac{1}{2}k_B T$ and solving for the temperature, we get

$$T = -\frac{\hbar\Gamma^2 + 4\hbar\delta^2}{8\delta k_B} \tag{1.22}$$

Finding the minimum of the above temperature with respect to detuning yields

$$\delta_{\text{optimal}} = -\frac{\Gamma}{2} \tag{1.23}$$

$$T_{\text{Doppler}} = \frac{\hbar\Gamma}{2k_B}. \tag{1.24}$$

We have shown that there is a lower bound to the temperature achievable via Doppler cooling, where the heating from the spontaneous emission events and the cooling process balance each other out. This lower bound is referred to as the Doppler limit T_{Doppler}. The

Doppler temperature for ^{39}K is reported to be 146 μK [21].

The recoil temperature T_{recoil}, from equation 1.11, and the Doppler temperature T_{Doppler} are related [20]

$$T_{\text{recoil}} = 4\varepsilon T_{\text{Doppler}}, \tag{1.25}$$

Where $\varepsilon = \frac{\Gamma}{\omega_{\text{recoil}}}$, and where ω_{recoil} is given by equation 1.12 [20].

1.2.3 Doppler Cooling of ^{39}K using the D_2 line

To effectively implement Doppler cooling, one would want a closed two-level system that enables continuous cycling of photons. While not fully closed, the D_2 line of ^{39}K is a good candidate for optical cycling. Addressing this transition, after the electrons are excited from the $4^2S_{1/2}\ \ (F = 2)$ state to the $4^2P_{1/2},\ \ (F' = 3)$ state, the selection rule $\Delta F = 0, \pm 1$ ensures that the electron decays back to $4^2S_{1/2},\ \ (F = 2)$, and we can repeat the cycle. However, since in $4^2P_{3/2}$, the $(F' = 2)$ state is only 21.1MHz away from $(F' = 3)$, occasionally, the closed cycle is broken and the electrons end up in this nearby state. From $F' = 2$, electrons sometimes decay to $4^2S_{1/2},\ \ (F = 1)$. To overcome this leaky closed cycle, we use a repump laser to drive $4^2S_{1/2},\ \ (F = 1)$ to $4^2P_{1/2},\ \ (F' = 2)$, after which the electrons can decay back to $4^2S_{1/2},\ \ (F = 2)$ and be reintroduced into the cycle [21].

1.2.4 Chirped Slowing

The atomic beam that the buffer gas source produces travels at about 150 m/s at peak velocity. This velocity is much lower than that of other traditional vapor sources. However, 150 m/s is still quite fast compared to the capture velocity of the MOT (50 m/s). In order

to slow this forward velocity to within the MOT capture range, we employ a technique known as chirped laser slowing. From equation 1.14, we know that an atom will scatter photons at the maximum rate when it is resonant with the light. So by red-detuning the laser beam that counter propagates to the atomic beam by about 262 MHz (beat note lock offset frequency), which is the Doppler shift for a 150 m/s velocity class, we can apply maximum force on atoms travelling at 150 m/s. But as these atoms slow, the effective detuning changes and hence the scattering rate decreases. To be able to address a wide range of velocity classes, and also account for the changing Doppler shift of the slowing atoms, one could sweep the frequency of the laser beam to counter the dynamic Doppler shift in time [24]. This method is often referred to as chirped slowing.

Since the $\delta_{\text{Doppler}} = -\vec{k} \cdot \vec{v}$, the rate of change of the Doppler shift is given by $\dot{\delta}_{\text{Doppler}} = -\vec{k} \cdot \vec{a}$. From equation 1.16, we can see that the maximum scattering force is $F_{\text{max}} = \hbar k \Gamma / 2$, and hence, the maximum acceleration is given by $a_{\text{max}} = \hbar k \Gamma / (2M)$. Since we would like the rate of change of our laser frequency to counter $\dot{\delta}_{\text{Doppler}}$, we have [20]

$$\begin{aligned} \dot{\omega}_{\text{laser}} &= -\dot{\delta}_{\text{Doppler}} \\ &= \vec{k} \cdot \vec{a} \\ &\leq \frac{\hbar k^2}{2\Gamma M}, \end{aligned}$$

where $\dot{\omega}_{\text{laser}}$ is the rate of the laser frequency sweep.

1.2.5 Magneto-Optical Trap

Although Doppler cooling provides a velocity-dependent force that slows the atoms down into a confinement region, without a position dependent force to push the atoms back toward the center of the trap, the cooled atoms will diffuse out of the trap eventually [23]. The spatially varying component of the force is produced by making use of the Zeeman effect. We first offer an overview of how a MOT employs the Zeeman effect to achieve simultaneous cooling and trapping. Later on, we detail the theory of the Zeeman effect including the hyperfine structure in ^{39}K. To produce cooling and restoring forces, a MOT utilizes a combination of three pairs of circularly polarized, counter-propagating beams of laser light, that are red-detuned compared to the transition frequency, as well as a pair of magnetic coils in an anti-Helmholtz configuration.

The anti-Helmholtz configuration simply refers to a configuration in which the current in the bottom and top coils have the same magnitude, but run in the opposite direction. The result is a quadrupole magnetic field which is zero at the center, where the atoms get trapped. The details of magnetic field calculation for the anti-Hemholz coils is presented in section 1.2.7, and as discussed, there we can reasonably assume that the magnetic field varies linearly in space near the center of the quadrupole. Considering only the z axis for now:

$$B(z) \propto z \tag{1.26}$$

The presence of the magnetic field causes the energy levels in an atom to split due to the Zeeman effect. The details of the energy shifts are presented in section 1.2.8, but for now we

just note the result [21]

$$E_{Zeeman}(z) = -g_F \mu_B m_F B(z), \tag{1.27}$$

where $g_{(f)}$ is the Lande g-factor (equation 1.31), $\mu_B = \frac{e\hbar}{2m_e}$ is the Bohr magneton, and m_F is the projection of the atom's total angular momentum F, along the z axis [21].

In reality, the MOT beams in our setup address the cycling transition from $F = 2$ to $F' = 3$. For simple illustrative purposes, we first consider a transition between two states with $F = 0$ and $F' = 1$.

In the presence of a linear magnetic field, the excited state with $F' = 1$ gets split into three states with $m_F = -1$, $m_F = 0$, and $m_F = 1$. The ground state with $F = 0$ does not get split. If the Lande-g factor is positive, then the states with positive m_F will shift higher in the positive z direction (direction of the applied magnetic field), while the states with negative m_F will shift down. The states with $m_F = 0$ do not shift in energy (see figure 1.3).

Considering only one dimension again, we have two counterpropogating MOT beams with opposite circular polarizations σ^+ and σ^- . Since angular momentum has to be conserved, the σ^+ beam can only excite electrons from $m_f = 0$ in the ground state, to $m_f = 1$ in the excited state [25]. Similarly the σ^- beam induces transitions from $m_f = 0$ of the ground state to $m_f = -1$ in the excited state.

Additionally the MOT beams are red-detuned relative to the transition from $m_F = 0$ in the ground state, to $m_F = 0$ in the excited state. The selectivity of transitions due to angular momentum conservation, along with the red-detuning of the beams, mean that each beam is resonant with its corresponding transition only on one side of the trap. Since we need to have a restoring force that pushes the atoms to the center, we place each of the

two σ^+ and σ^- beams such that they point to the center of the trap, on the side where they are on resonance. Such a configuration is shown in Fig. 1.3

As an example, let's consider what happens when an atom starts moving out from the center. If this atom moves to the right, it will experience a linear red shift in its $m'_F = -1$ state. At some point, the σ^- beam which is also red detuned will be on resonance with the $m_F = 0$ to $m' = -1$ transition. When a photon from this σ^- beam gets absorbed, the atom will receive a momentum kick toward the center of the trap, since the σ^- beam is pointing to the left. At the same time, the $m' = +1$ state is getting blue shifted as we move to the right. As a result, the σ^+ beam moves further and further out of resonance, which fortunately for us, means that our atom is not likely to receive a momentum kick that pushes it out of the trap!

So far, we haven't discussed the Doppler effect in this setup, but based on our discussion in section 1.2.1, we are fortunate again, since the Doppler effect works in our favor as well, and provides cooling!

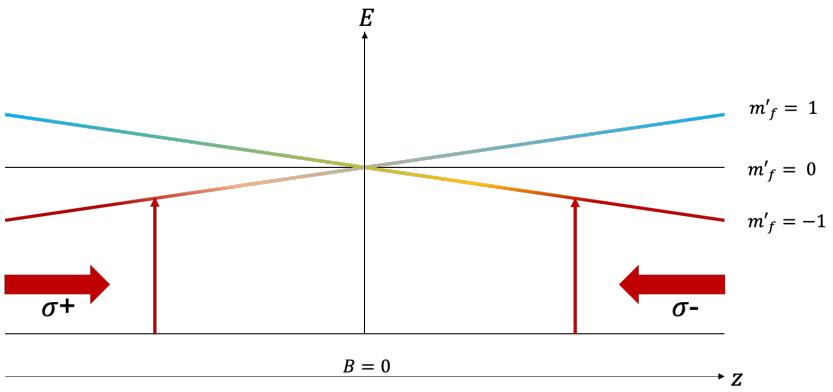

Figure 1.3: 1-Dimensional representation of a MOT: The combination of counter-propagating, red-detuned laser light, and the Zeeman effect produced by a magnetic field, create a MOT achieving simultaneous cooling and trapping.

So far, we considered the simple case of the Zeeman effect and its use to produce a MOT,

in an atom with an $F = 0$ ground state. However, the cycling transition used in ^{39}K has a ground state with $F = 2$, and an excited state with $F' = 3$. This means that the Zeeman effect will split the ground state into five levels with $-2 \leq m_f \leq 2$, and the excited state, into seven levels with $-3 \leq m_f \leq 3$. The transitions that the MOT beams would address will look like figure. 1.4.

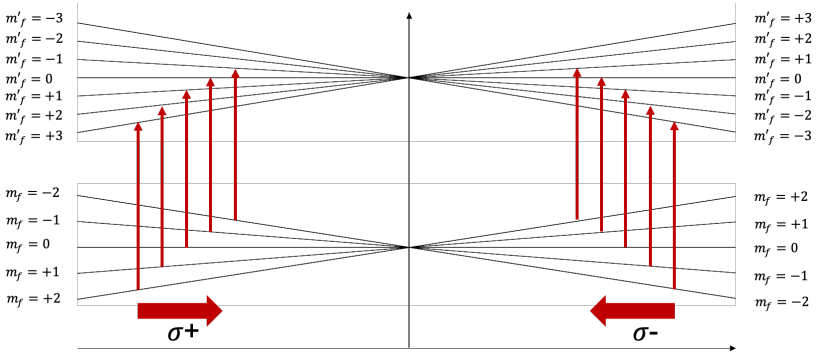

Figure 1.4: 1-Dimensional representation of the Zeeman splittings and transitions for the D-2 line of ^{39}K

1.2.6 Anti-Helmholtz Magnetic Field for a MOT

The magnetic field for the MOT is created using two sets of coils with equal currents that run in opposite directions as shown in figure 1.6. This configuration is referred to as the anti-Helmholtz configuration, and it produces a quadrupole field, which is zero at the center. It makes sense that we need a zero magnetic field at the center, since atoms will not feel a net force from the lasers described in section section 1.2.5 in this position, and will be trapped there.

We use a stack of two coils with ten turns for each of the top and bottom sets. For simplicity, I will first describe what the magnetic field from two single loops in Anti-Helmholtz configuration looks like. Later, we will extend the calculation using a simulation to explore

the magnetic field that will be produced by the two sets of doubly-stacked concentric coils.

1.2.7 Magnetic Field From Anti-Helmholtz Loops

We first calculate the magnetic field of a single loop of current on its central axis. We use the Biot-Savart law:

$$\vec{B} = \frac{\mu_0 I}{4\pi} \int \frac{d\vec{l} \times \hat{r}}{r^2},$$

where μ_0 is the permeability constant and I is the current in the loop. Additionally, $\hat{r}$ represents a unit vector in the direction of $\vec{r}$, the vector connecting the current element $d\vec{l}$ and the point at which we are evaluating the magnetic field.

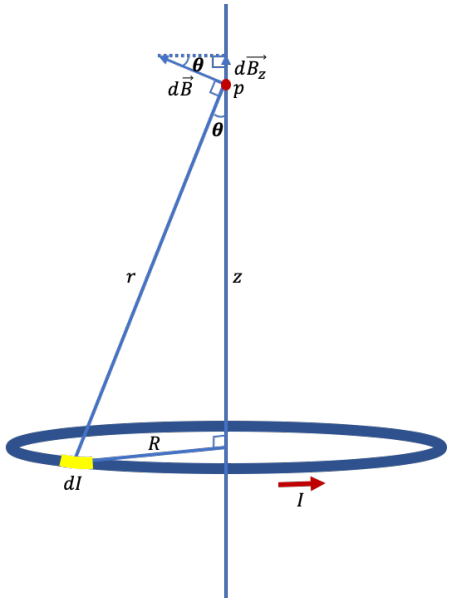

Figure 1.5: Magnetic field from a current element of a loop on the main axis.

Considering figure 1.5, we note that the cylindrical symmetry of the setup means that all components of the magnetic field besides the z component cancel on axis, and we only need

to integrate along the loop to add up the z components:

$$\begin{aligned} B(z)_z &= \frac{\mu_0 I}{4\pi} \sin(\theta) \int \frac{dI}{r^2} \\ &= \frac{\mu_0 I}{4\pi} \int \frac{R\, dI}{r^3} \\ &= \frac{\mu_0 I}{4\pi} \int \frac{R\, dI}{(R^2 + z^2)^{3/2}} \\ &= \frac{\mu_0 I}{2} \frac{R^2}{(z^2 + R^2)^{\frac{3}{2}}} \end{aligned}$$

Now we can consider the magnetic field from two coils in an anti-Helmholtz configuration, as shown in figure 1.6. We simply need to add the contribution from each coil, with an extra minus sign, to account for the opposite direction of the magnetic field with respect to the z axis:

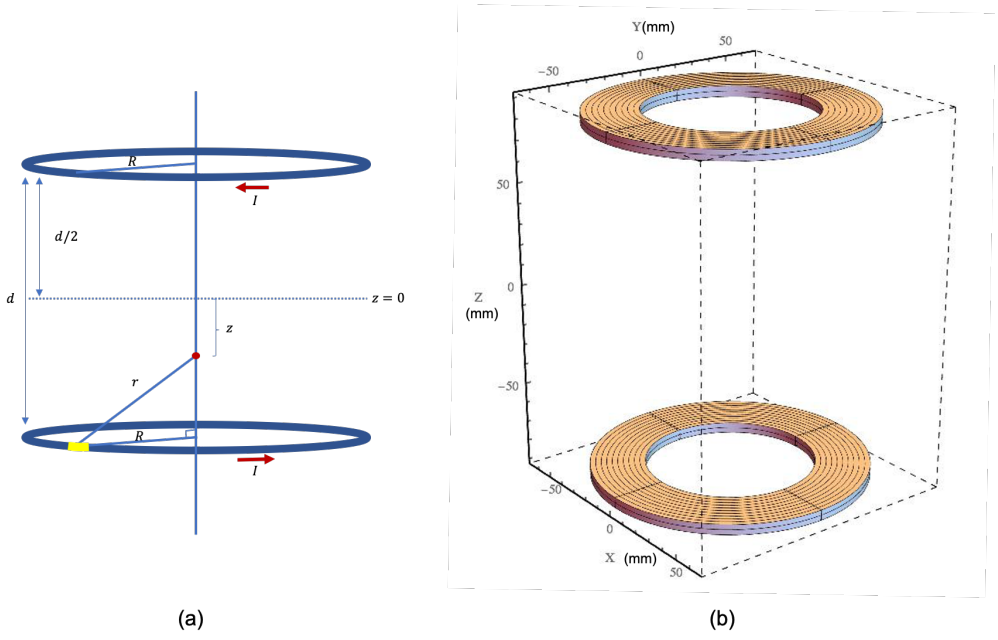

Figure 1.6: (a) Two loops of current, in anti-Helmholtz configuration. (b) Schematic of magnetic coils used in our experiment. Each set is a double-stack of coils with ten turns each.

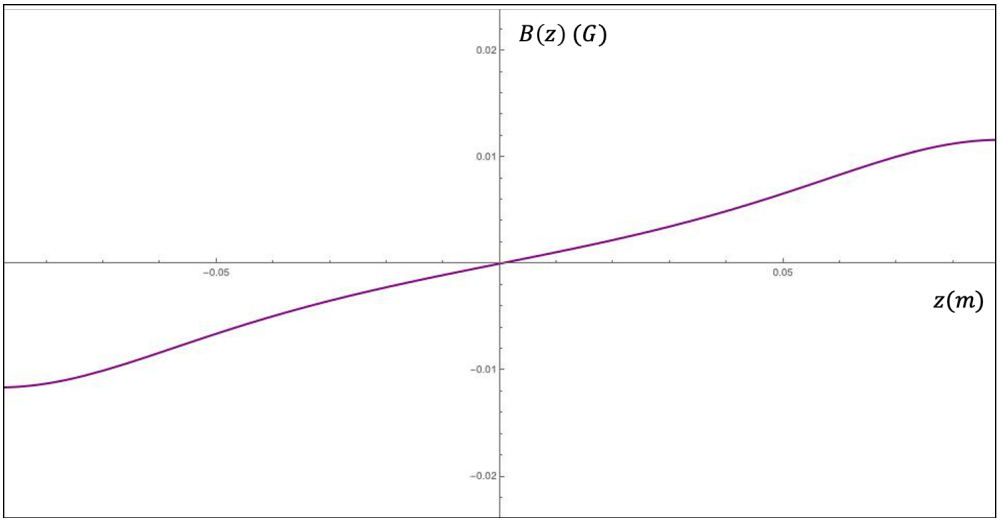

Figure 1.7: The magnetic field of two loops of current in an anti-Helmholtz configuration, as a function of distance on the z-axis. We have used the following values for the parameters in equation 1.28: $I = 2A, d = 0.175m, R = 0.05m$

$$B_a(z) = \frac{\mu_0 I R^2}{2}\left[\frac{1}{((\frac{d}{2}+z)^2+R^2)^{\frac{3}{2}}} - \frac{1}{(\frac{d}{2}-z)^2+R^2)^{\frac{3}{2}}}\right] \tag{1.28}$$

This expression is graphed in figure figure 1.7. We note that the magnetic field varies almost linearly near the point halfway between the two coils.

This model, however, is a simplification of the magnetic coils used in our experiment. We use two stacks of 10 coils for each of the top and bottom magnetic field generators. In this setup, the thickness of the wires becomes significant, and the field calculations become tedious to carry out manually. Instead, we have modeled the magnetic field using the Mathematica simulation package Radia [26]. The resultant magnetic field plot from the simulation is shown in figure 1.8. We have measured the magnetic field gradient to be 0.16 G/cm/A along the z direction and 0.08 G/cm/A radially. We run the magnetic field coils

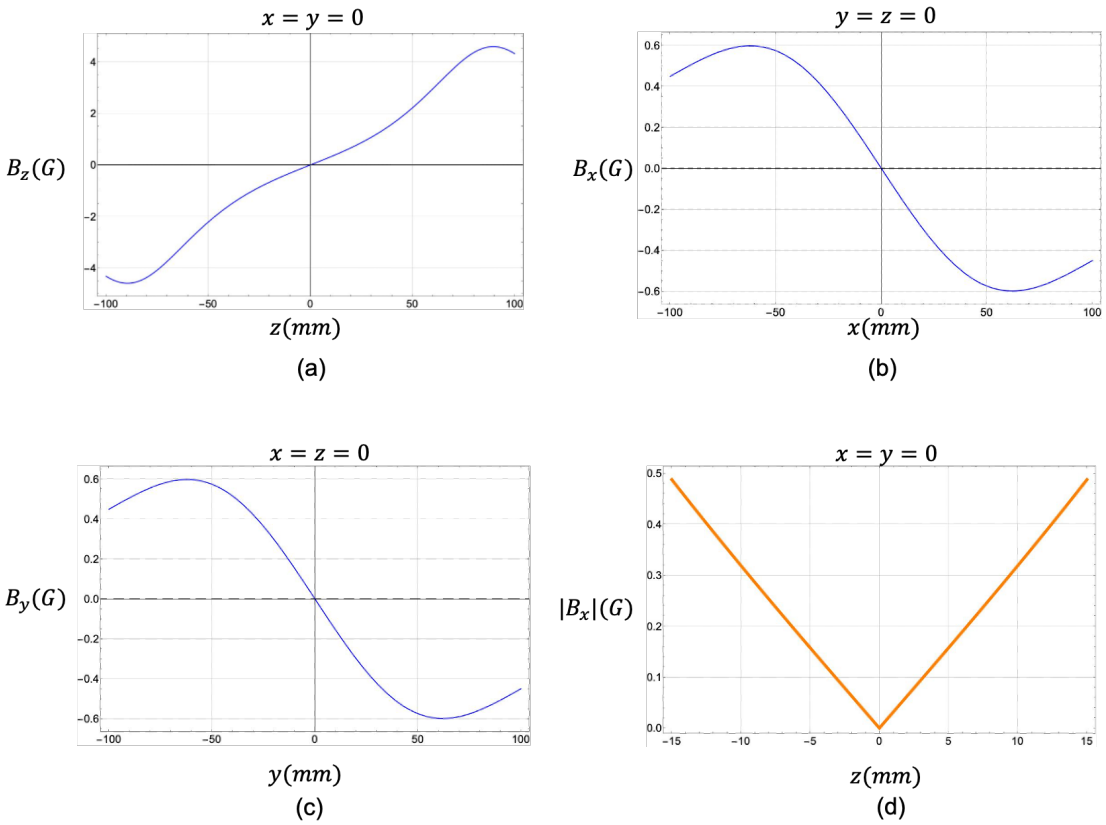

Figure 1.8: The magnetic fields from the set of coils represented in figure 1.4, as produced by the Mathematica simulation package Radia. All distances are shown in mm, and all magnetic fields are represented in units of gauss. (a) The z component of the magnetic field on the z-axis. Note that the magnetic field is almost linear near the center. (b, c) The x and y components of the field on the x and y axes, respectively. Even though we did not explicitly derive an expression for these two components, the simulation clearly shows a field that is nearly linear near the center. (c) is a plot of the norm of the field, $B = \sqrt{B_x^2 + B_y^2 + B_z^2}$, in the vicinity of $z = 0$ on the z axis.

with 50 A of current, which gives us a maximum gradient of 8 G/cm.

1.2.8 Zeeman Effect in Alkalis

Earlier in section 1.1.4 we discussed the hyperfine structure of ^{39}K in the absence of external magnetic fields. The presence of an external magnetic field, such as the one generated by the MOT coils, causes further splittings of the energy levels. This effect, termed the Zee-

man effect, arises from interactions between this external magnetic field with the electron and nuclear spins [17].

Our goal in this section is to discuss the Zeeman effect in more detail. While the more qualitative description in section 1.2.5 suffices for a general understanding of how a MOT functions, the following section is included for readers who are curious about the mathematical background behind the Zeeman effect. We will follow the derivations and explanations in [14], and [17] closely, in the following discussions of the Zeeman effect.

When an atom is placed in an external magnetic field, the interaction Hamiltonian can be written as

$$H_B = -\frac{\boldsymbol{\mu}_{\text{total}} \cdot \mathbf{B}}{\hbar},$$

where $\boldsymbol{\mu}_{\text{total}}$ represents the total magnetic moment of the atom. Since we need to consider the interaction of both the nuclear magnetic moment and the total electronic magnetic moment with this external field, $\boldsymbol{\mu}_{\text{total}}$ can be written as [14]

$$\begin{aligned}\boldsymbol{\mu}_{\text{total}} &= \boldsymbol{\mu}_J + \boldsymbol{\mu}_I \\ &= -g_J \mu_B \mathbf{J} + g_I \mu_N \mathbf{I}.\end{aligned}$$

Note the difference in sign for the two terms above. The reason that a positive sign is used for the nuclear magnetic moment term, is that g_I can be either positive or negative, based on the nuclear structure of the atom [14]. The second term in the expression for the total magnetic moment can be ignored, since $\mu_N = \frac{m_e}{m_N}\mu_B$ [17], and the small mass ratio makes $\mu_N \ll \mu_B$ [14].

For calculating the energy eigenstates of the Hamiltonian, we should first consider what quantum numbers are "good," and can be used for our eigenbasis. We carry out this consideration for the three cases of weak, intermediate and strong fields.

1.2.9 Weak Field Zeeman Effect

If the hyperfine interaction is much stronger than the interaction of the external magnetic field with the system, the eigenstates will be dominated by the hyperfine interaction. As a result, $|F, m_f\rangle$ form an eigenbasis, while J and m_J are not "good" quantum numbers [14]. Under these conditions, the Hamiltonian can be written as [14]

$$H = -g_F \mu_B \mathbf{F}.\mathbf{B} \tag{1.29}$$

Which gives energy levels as [4]:

$$E = g_F \mu_B B m_F \tag{1.30}$$

Where g_F is the g-factor for total spin, obtained using the projection theorem (more detailed explanation can be found in [14])

$$g_F = \frac{F(F+1) + J(J+1) - I(I+1)}{2F(F+1)} g_J. \tag{1.31}$$

1.2.10 Strong Field Zeeman Effect

If the interaction of the magnetic field with the system is stronger than the hyperfine interaction, we can no longer use $|F, m_F\rangle$ as our eigenbasis [17]. Instead, the interaction be-

tween the magnetic field and the total orbital angular momentum of the electron will dictate the main energy levels, with the hyperfine effects presenting perturbations to this main system [14]. As a result, we can use $|I, J, m_I, m_J\rangle$ as the eigenbasis for our calculations [14]. Since the hyperfine Hamiltonian in equation 1.4 is already in the basis of $|I, J, m_I, m_J\rangle$, we can simply use it as our perturbation Hamiltonian

$$H' = A_{\text{hfs}} \mathbf{I} \cdot \mathbf{J}.$$

The first order energy corrections using perturbation theory would give us the energy splittings as

$$E' = \langle I, J, m_I, m_J | H' | I, J, m_I, m_J \rangle.$$

Assuming that the magnetic field is along the z-direction, the above expression evaluates to [14]

$$E' = A m_I m_J. \tag{1.32}$$

The total energy of each level is the sum of this Zeeman energy correction, and the energy $g_J m_J B m_J$ from the interaction of the total angular momentum of the electron with the magnetic field. Thus, the total energy for each level can be written as [14]

$$E_{\text{total}} = g_J \mu_J B m_J + A m_I m_J. \tag{1.33}$$

1.2.11 Intermediate Zeeman Effect

The Zeeman effects described in the previous two sections are only extreme cases. It is possible to have a magnetic field such that its interaction with the electron is on the same order as the hyperfine interaction. In such intermediate cases, obtaining the energy eigenstates is not as easy as before and requires direct diagonalization of the Hamiltonian. Details of such calculation are beyond the scope of this thesis but can be found in [14].

2

Spectroscopy and Laser Locking

2.1 Spectroscopy and Laser Locking

In this section we will describe the theoretical background necessary to understand our laser locking scheme. We use a mixture of Doppler free saturated absorption spectroscopy and modulation transfer spectroscopy to lock our reference laser. We use an offset-locking scheme to lock the MOT laser, using the already-locked reference laser as a reference. I will go into the details of the experimental setup for the above schemes in chapter 3. We will start by discussing Doppler broadening of transition lines, the challenges it presents and the reason why we use Doppler-free saturated absorption spectroscopy. Next, we will discuss

how saturated absorption spectroscopy and modulation transfer spectroscopy work.

As we discussed in chapter 1, the methods that we use for cooling and trapping the atoms are highly frequency dependent. As a result, it is necessary to have a laser system with a frequency linewidth less than that of the electronic transition used to obtain the MOT. This frequency stabilization is referred to as "locking" the laser. One way to lock the laser frequency is to employ spectroscopy to stabilize the laser referenced to an electronic transition. In our case, we would like our laser linewidth to be less than that of the D2 line of ^{39}K which has a linewidth of $\approx$ 6 MHz (see section 1.1.3).

In spectroscopy, a light beam with a frequency corresponding to that of a certain electronic transition is used to excite atoms in a medium, in our case a potassium vapor cell. When light passes through this vapor cell, some of the photons at the resonant frequency are absorbed. Hence, by looking at the intensity profile of the outgoing beam as a function of frequency, we will be able to identify a dip corresponding to the resonant frequency. Our goal is to be able to lock our laser to such an absorption feature.

2.1.1 Doppler Broadening of Transitions

It turns out that the simple spectroscopy idea described above would not give us a narrow enough laser linewidth to make a MOT. The reason for this lack of resolution lies in the thermal motion of the atoms that are being addressed with the laser. If every atom in the vapor cell were at rest, then only photons of the right frequency (the desired transition frequency, up to the transition linewidth) would get absorbed. However, since these atoms have a finite temperature, their velocities have a spread consistent with the Maxwell-Boltzmann distribution. As a result, each moving atom experiences a Doppler shift in

the frequency of the photons that it "sees " (refer to section 1.2.1 for more detail on the Doppler effect). This means that some of the photons that are not at the transition frequency for an atom at rest are "seen" as having the right frequency by the moving atoms, and are therefore absorbed. This effect will broaden the transition feature in the absorption spectrum, resulting in an unresolved absorption peak that is not sharp enough for a MOT laser. Typically, it is possible to lock the laser with a resolution of up to 1/10th of the the broadened feature. The Doppler linewidth for potassium atoms at 4K is $\sim$ 250 MHz (see equation 2.2), which can be compared to the D2 transition linewidth of $\sim$ 6 MHz. We can derive the broadened spectrum shape by considering the fraction of atoms that would absorb light at frequencies in the range ω to $\omega + d\omega$. The frequencies are related to the velocities through the Doppler shift relation $\frac{\delta}{\omega_0} = \frac{v}{c}$, where δ is the detuning from the transition frequency ω_0 [14]. Thus, we can consider the fraction of atoms moving with velocities between v and $v + dv$, given by the Maxwell-Boltzmann distribution [14]

$$f(v)dv = \sqrt{\frac{M}{2\pi k_B T}}\exp\left(-\frac{Mv^2}{2k_B T}\right)dv.$$

Using the Doppler relation to substitute for the velocities, we can get the expression in terms of frequencies [14]

$$g_D(\omega) = \frac{c}{u\omega_0\sqrt{\pi}}exp\left(-\frac{c^2}{u^2}\left(\frac{\omega-\omega_0}{\omega_0}\right)^2\right), \tag{2.1}$$

Where g_D is the Gaussian broadened spectrum, $u = \sqrt{2k_B T/M}$, and the maximum occurs at $\omega = \omega_0$ [14]. The value of the maximum is then

$$g_{D,max} = \frac{c}{u\omega_0\sqrt{\pi}}.$$

Hence, to calculate the full width at half maximum (FWHM), we have to solve the following equation for ω:

$$g_D(\omega) = \frac{c}{2u\omega_0\sqrt{\pi}},$$

which reduces to [14]

$$\ln 2 = \frac{c^2}{u^2}\left(\frac{\omega - \omega_0}{\omega_0}\right)^2.$$

The ratio of the FWHM to the center, (ω_0), is then [14]

$$\frac{\text{FWHM}}{\omega_0} = \frac{2(\omega - \omega_0)}{\omega_0} = 2\sqrt{\ln 2}\frac{u}{c}. \tag{2.2}$$

This Doppler broadened spectrum is depicted in figure 2.1. For ^{39}K, the Doppler widths at 300K and 4K are $\sim$ 2 GHz and $\sim$ 250 MHz respectively.

2.1.2 Doppler-Free Saturated Absorption Spectroscopy

It is possible to avoid Doppler-broadened spectra and resolve transition absorption peaks by implementing Doppler-free saturated absorption spectroscopy. In Doppler-free spectroscopy, two counter-propagating beams of the same frequency, one named "pump" and

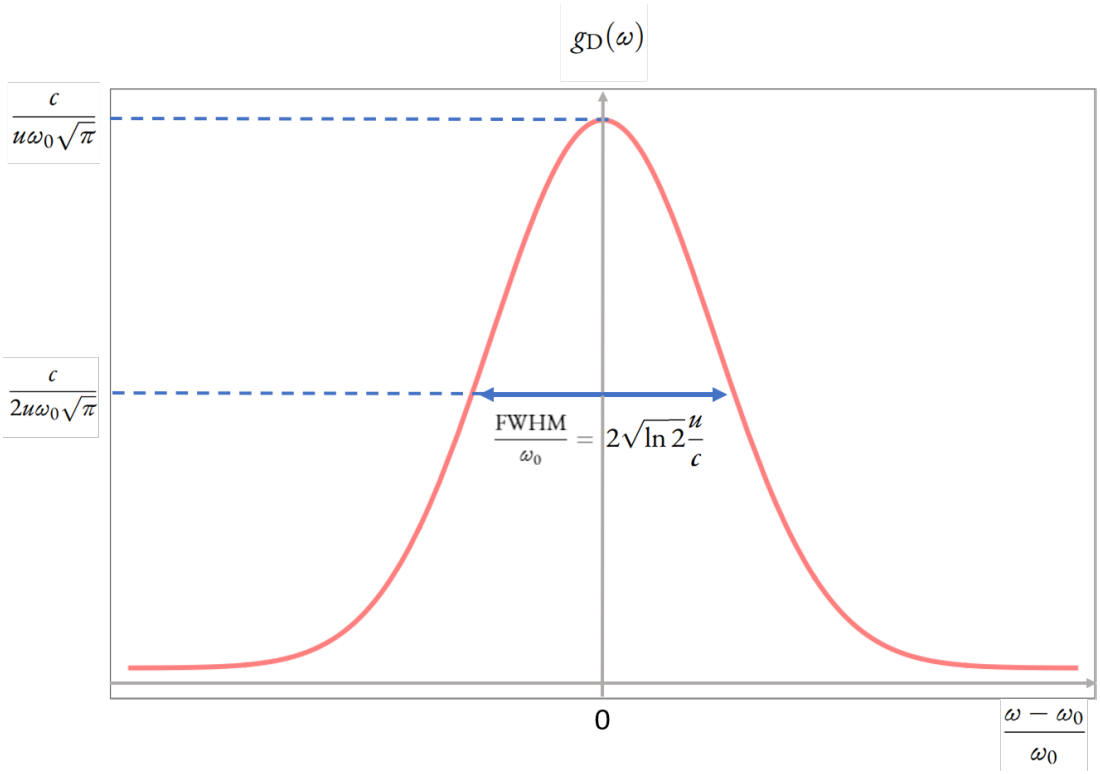

Figure 2.1: Gaussian profile of a Doppler-broadened spectrum. Here, $u = \sqrt{2k_BT/M}$ [14].

the other "probe," pass through an atom vapor cell (potassium, in our case) in a counter-propagating fashion. The frequency of the two beams is simultaneously scanned around the transition frequency and the intensity of the probe beam is monitored [27]. During the scan, when the laser beams are detuned with respect to the transition frequency, each laser is resonant only with atoms of a specific non-zero velocity class. Since the two beams are counter-propagating and have the same frequency, the atoms that they address have the same speed, but move in opposite directions. As a result, at all nonzero velocities, the two beams are addressing separate classes of atoms, and their absorption profiles are independent of one another (figure 2.2 (a)). However, when the frequency of the laser is on reso-

nance, both lasers address the atoms that are at rest with respect to the beam propagation axis [27]. As a result, the pump and the probe will be competing for absorption. Usually, the intensity of the pump is higher than that of the probe, and thus the probe will not be able to cause that many transitions compared to the pump. The result appears as a peak in the intensity (or a dip in absorption) of the probe at the transition frequency. Since this feature is caused by the zero-velocity class, the Doppler effect no longer poses an issue. In this case, the width of the Doppler-free feature is set by the natural linewidth.

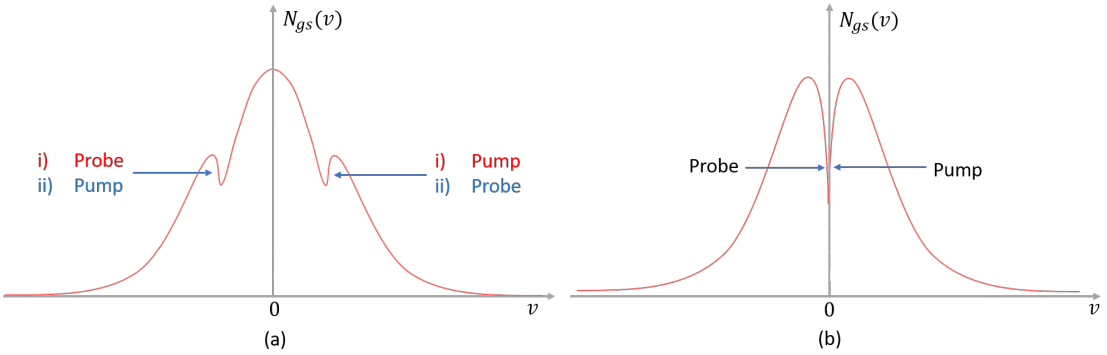

Figure 2.2: Number of atoms of each velocity that exist in the ground state N_{gs} is plotted as a function of velocity. Positive velocity is defined as being in the same direction as the propagation of the probe beam. **(a)** When the pump and probe beams are detuned with respect to the transition frequency, they address two separate velocity classes of the same speed that move in opposite directions. **i)** indicates the case where pump and probe are red detuned with respect to the transition frequency. **ii)** indicates the case where pump and probe are blue detuned with respect to the transition frequency. **(b)** When pump and probe are resonant with the transition frequency, they both address the class of atoms that are at rest. In this case pump and probe compete for the transition. Figures inspired by and partially replicated from [28]. The absorption signal from these cases appear as figure 2.3.

2.1.3 The Crossover Peak

So far, we have only considered a two-level system. The absorption profile gets more complicated if we have additional transitions that fall within the Doppler width[29]. Let's consider the case of having two transitions with frequencies ω_1 and ω_2 with a common

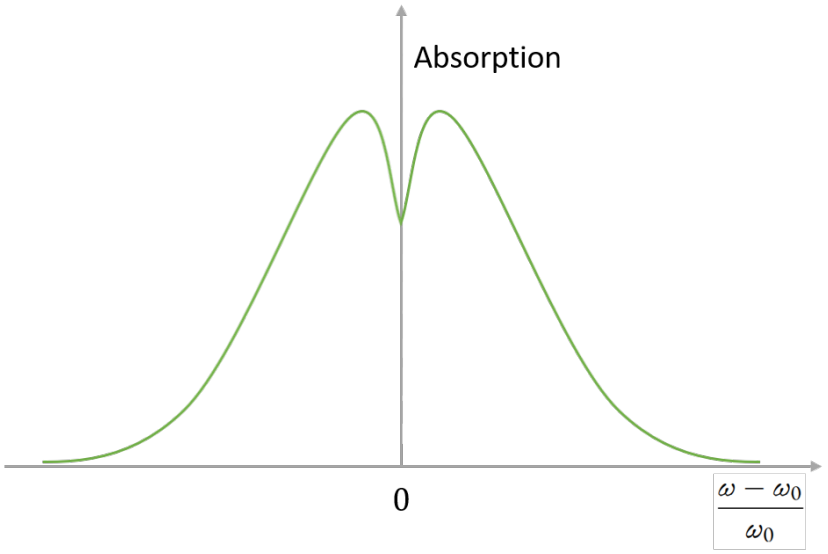

Figure 2.3: Absorption of the probe beam (arbitrary units) plotted as a function of detuning in saturated absroption spectroscopy. When the laser is on resonance (no detuning case), the pump and probe address the same velocity classes and compete for exciting the electrons from the ground state. The result is a strong dip in the absorption signal.

ground state, such that $\omega_1 < \omega_2$. When both the probe and pump frequencies are at ω_1, they will both address the zero-velocity class and we will get the regular absorption feature that we described above. Similarly, both beams address the zero-velocity class when resonant with the second transition. Now, let's consider an intermediate frequency ω_c, such that $\omega_1 < \omega_c < \omega_2$. When at ω_c, the two beams are blue-detuned with respect to ω_1 and red-detuned with respect to ω_2. Let's consider the pump beam first. At an arbitrary ω_c, there is a certain class of atoms with speed v_1 moving toward the pump that will "see" the beam as resonant with transition 2 due to the Doppler effect. At the same time, there is another class of atoms with speed v_2 moving away from the pump, that will "see" the pump as being resonant with transition 1. Generally, $v_1 \neq v_2$. However, when $\omega_c = (\omega_1 + \omega_2)/2$, the two classes of atoms would be moving in opposite directions but with $v_1 = v_2$. At this

frequency of ω, the probe beam will address the same class of atoms, except for the fact that the atoms that are addressed by the pump for transition 1 will be addressed by the probe for transition 2, and vice versa [29]. The result is again a competition between pump and probe to excite electrons from the ground state, but this time to different excited states. The effect appears on the probe intensity profile as a strong dip.

In the case where there is a common excited state, the effect appears as a peak in intensity at the crossover frequency due to stimulated emission [30]. ^{39}K has a crossover feature of this type, since the various hyperfine transitions of the D2 line of ^{39}K are from $|F = 1\rangle \rightarrow |F' = 0, 1, 2\rangle$, and from $|F = 2\rangle \rightarrow |F' = 1, 2, 3\rangle$ [31]. This feature is again strong and unaffected by the width of the thermal distribution. We use this feature as a frequency locking point for our reference laser.

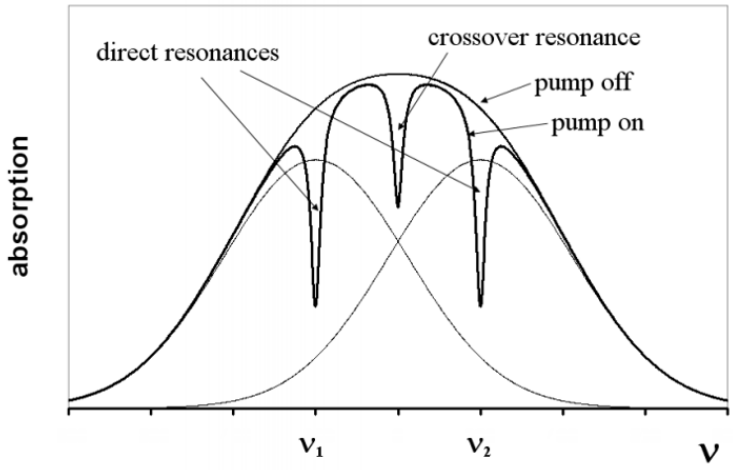

Figure 2.4: Absorption profile of a three level system, with a common ground state, plotted as a function of frequency. The crossover resonance happens when the laser frequency is equal to the average of the two transition frequencies. Image from [32].

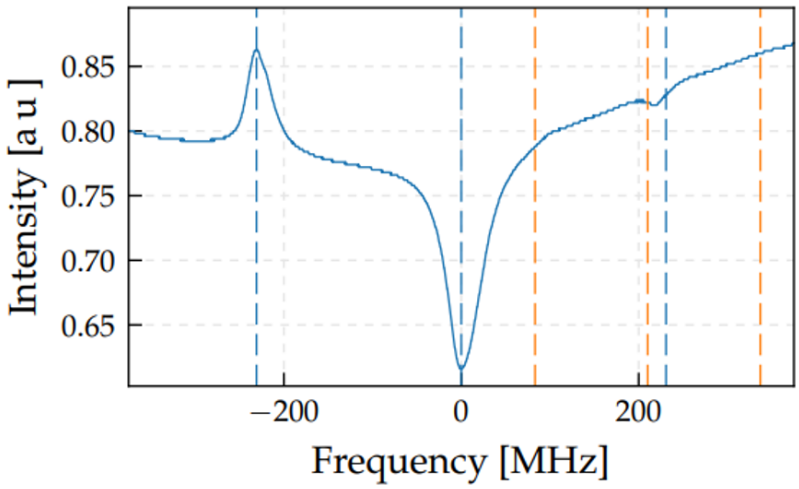

Figure 2.5: Saturated absorption spectroscopy transmission profile of ^{39}K D2 line. The peak on the right hand side represents transitions from $|F = 1\rangle \rightarrow |F' = 0, 1, 2\rangle$, the peak on the left represents transitions from $|F = 2\rangle \rightarrow |F' = 1, 2, 3\rangle$, and the middle dip in transmission represents the crossover frequency for the shared excited states. The blue dashed lines represent transitions for ^{39}K, and the orange lines represent those of ^{41}K. Image and description from [31].

2.2 Modulation Transfer Spectroscopy

So far, we have discussed how, with Doppler-free spectroscopy, we are able to resolve the transition lines and use them as reference points to lock our lasers to (section 2.1.2). However, we have not discussed the procedure for locking the lasers to these transitions. The locking process involves generating an error signal that indicates how far the laser frequency is from the desired frequency. Modulation transfer spectroscopy (MTS) will provide us with the error signal. This error signal is then fed into a proportional-integral-derivative (PID) controller, which will provide a feedback signal to the laser to push the laser frequency to the desired value.

The procedure involves modulating the pump beam to create frequency side bands,

transferring these side bands to the probe beam to generate a beat signal, mixing the signal with another radio frequency (RF) signal at the modulation frequency, and using a phase detector that will extract the error signal from the mixed signal.

We will outline the theory behind each of these steps below. A schematic of the setup is shown in figure 2.6.

2.2.1 Modulation Transfer

In this section, we will closely follow [27, 33]. Let us denote the frequency of the pump beam by f_{pump}. This frequency is often referred to as the carrier frequency. In the MTS scheme, we first modulate the pump beam using an electro-optic modulator (EOM) that receives an RF input at the modulation frequency f_{mod}. This modulation creates two frequency side bands at $f_{\text{pump}} + f_{\text{mod}}$ and $f_{\text{pump}} - f_{\text{mod}}$ on the pump beam. This modulation can be written as [27]

$$\begin{aligned} E &= E_0 \sin\Big(2\pi f_{\text{pump}} t + \Delta \sin\left(2\pi f_{\text{mod}} t\right)\Big) \\ &= E_0\Big[\sum_{j=0}^{\infty} J_j(\Delta) \sin\Big(2\pi(f_{\text{pump}} + n f_{\text{mod}})t\Big) + \sum_{j=0}^{\infty} (-1)^n J_j(\Delta) \sin\Big(2\pi(f_{\text{pump}} - n f_{\text{mod}})t\Big)\Big]. \end{aligned}$$

Here, Δ represents the modulation order, and the $J_n(\Delta)$ are Bessel functions of order n [27]. Since we care about limit where f_{pump} is strong with two side bands at $f_{\text{pump}} + f_{\text{mod}}$ and $f_{\text{pump}} - f_{\text{mod}}$, $\Delta < 1$ and the above equation can be approximated as [27]

$$E \approx E_0\Big[J_0(\Delta) \sin\left(2\pi f_{\text{pump}}\right)t + J_1(\Delta)\big(\sin\left(2\pi(f_{\text{pump}} + f_{\text{mod}})t\right)\big) - \sin\left(2\pi(f_{\text{pump}} - f_{\text{mod}})t\right)\big)\Big].$$

Next, the pump beam passes through the potassium vapor cell. Here, the pump and probe beam are aligned such that they are counter-propagating. Recall that aside from the side bands, the pump and the probe beams have the same frequencies ($f_{\text{pump}} = f_{\text{probe}}$). Through a non-linear process known as four-wave mixing, some of the side bands on the pump beam get imprinted on the probe beam [27, 33]. The details of this process are described in [34], but are beyond the scope of this thesis. The imprinted side bands on the probe beam will beat with the main frequency f_{probe}. A photodiode that monitors the probe beam will then pick this beat signal which has the following form [27, 33]:

$$S_{\text{beat}}(f_{\text{mod}}) \propto \frac{J_0(\Delta)J_1(\Delta)}{\sqrt{\Gamma^2 + 2\pi f_{\text{mod}}^2}}\big[(L_{-1} - L_{-1/2} + L_{1/2} - L_1)\cos(2\pi f_{\text{mod}}t + \varphi) \\ +(D_1 - D_{1/2} - D_{-1/2} + D_{-1})\sin(2\pi f_{\text{mod}}t + \varphi)\big], \tag{2.3}$$

where [27, 33]:

$$L_n = \frac{\Gamma^2}{\Gamma^2 + (\delta - 2\pi n f_{\text{mod}})^2},$$
$$D_n = \frac{\Gamma(\delta - 2\pi n f_{\text{mod}})}{\Gamma^2 + (\delta - 2\pi n f_{\text{mod}})^2},$$

Γ is the linewidth of the transition, δ is the detuning, and φ is an arbitrary phase [27, 33]. The beat signal (equation 2.3) contains a sine and a cosine term that have the same argument. Hence, by varying φ it is possible to have either term vanish or to get a mixture of the two. The phase is thus a knob that allows adjusting of the beat signal.

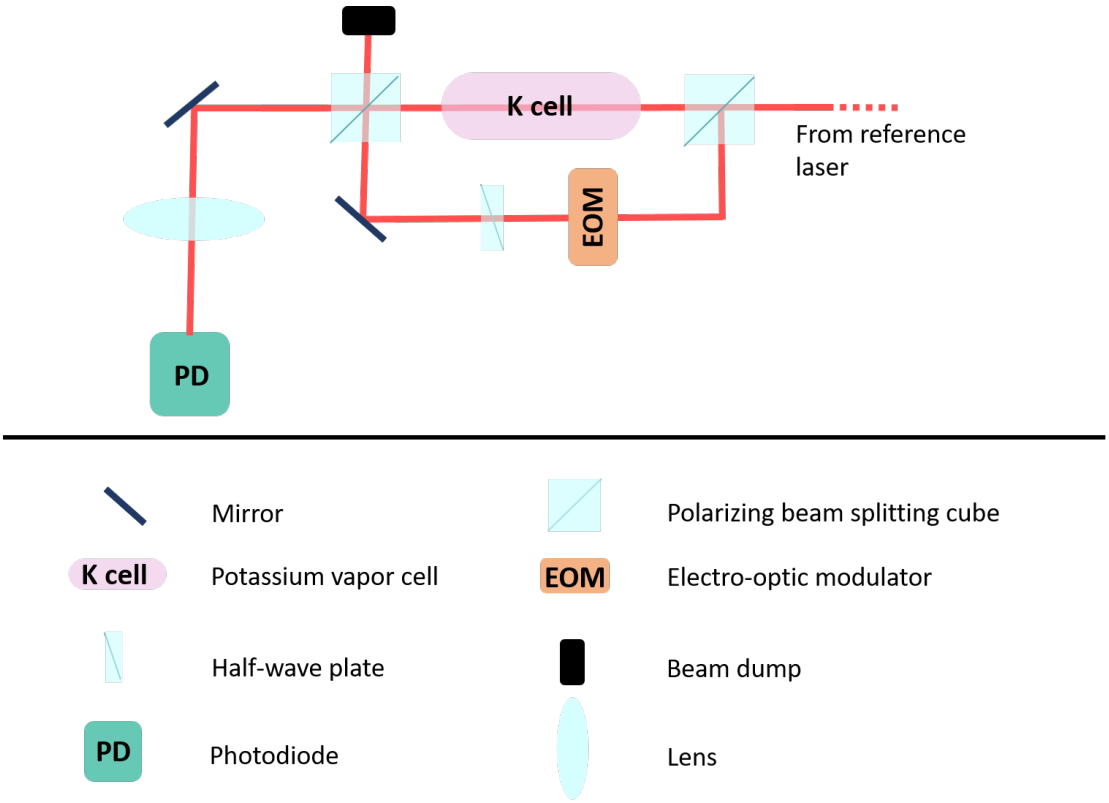

Figure 2.6: Schematic of the modulation transfer spectroscopy setup. The reference laser beam is split into two branches. One branch (pump) is passed through an EOM to acquire sidebands, and is then passed through the potassium vapor cell. The other branch (probe), directly passes through the potassium vapor cell, counter-propagating with the pump. The probe beam is monitored using a photodiode.

2.2.2 Demodulation and Error Signal Generation

As discussed above, we would like to have control over φ so that we can pick a desired combination of the two terms in equation 2.3. To do so we send the signal from the photodiode to a demodulation circuit. The photodiode signal is first amplified and is then mixed with another RF signal that has the same frequency as the modulation frequency, but is shifted by some phase φ_{demod}. The result is then passed through a low pass filter. Setting φ_{demod} allows for selecting a desired error signal. The error signal is then sent to a PID con-

troller that sends feedback to the laser to keep it "locked" to the zero crossing of the error signal.

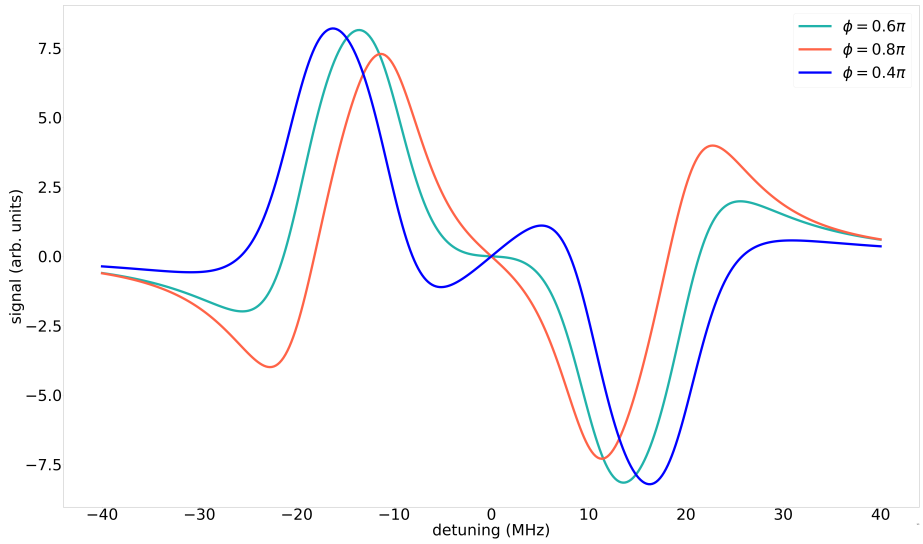

Figure 2.7: Error signal of modulation transfer spectroscopy based on equation 2.3. For this plot, $\Gamma = 2\pi \times 6.035$ MHz, and $f_{\text{mod}} = 20$ MHz.

2.2.3 Experimental Implementation

In order to lock our reference laser to the crossover feature of the D2 line of ^{39}K, we first split the reference laser beam into two branches. One branch is passed through an EOM to acquire sidebands (pump), and is then passed through the potassium vapor cell. The EOM receives a signal at 20 MHz from a Rigol DG1022 waveform generator. The other branch of the reference laser beam (probe) directly passes through the potassium vapor cell, counter-propagating with the pump. The probe beam is monitored using a photodiode. The photodiode beat signal (equation 2.3) is passed through a Minicircuits BLP-10.7+ low-

pass filter, and then through a ZFBT-4R2GW-FT+ bias tee that will separate out the DC component of the signal. The oscillatory portion of the signal is then amplified using two ZFL-500LN+ low- noise amplifiers. The result is sent to a phase detector that receives a phase-delayed 20 MHz signal from the same waveform generator that drives the EOM. The phase detector generates an error signal that is monitored on an oscilloscope and is also sent to a PID controller that provides feedback to the reference laser (Toptica TA Pro). A schematic of this setup is shown in figure 2.8.

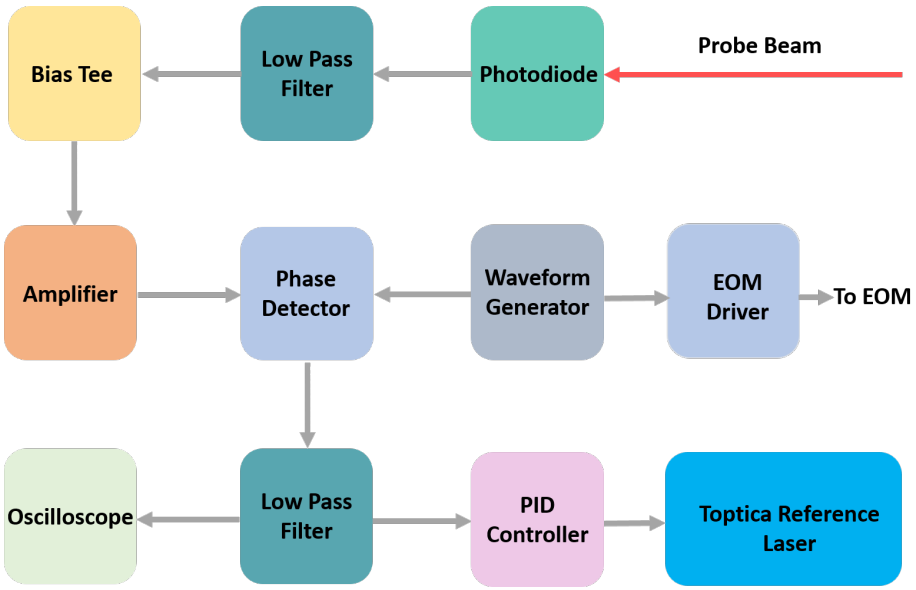

Figure 2.8: Schematic of the demodulation circuit used in our modulation transfer spectroscopy setup. For detailed description of components refer to section 2.2.3.

2.3 Frequency Offset Locking

With Doppler-free spectroscopy, we are able to lock our laser to the crossover frequency. However, sometimes we need a laser lock with a slight offset compared to the crossover frequency. One way to achieve this result is by beat note offset locking. In this scheme two

lasers are used, one which is already locked to a certain frequency using a method such as Doppler-free spectroscopy, and a second laser that will be offset locked to the first laser. To illustrate this scheme let's call the already-locked laser the "reference" laser, and the laser that we would like to offset-lock the "MOT" laser. A schematic diagram of the optics setup for beat note locking is shown in figure 2.9. The electronic components are shown in figure 2.10. We modulate the frequency of the reference laser by passing it through an AOM.

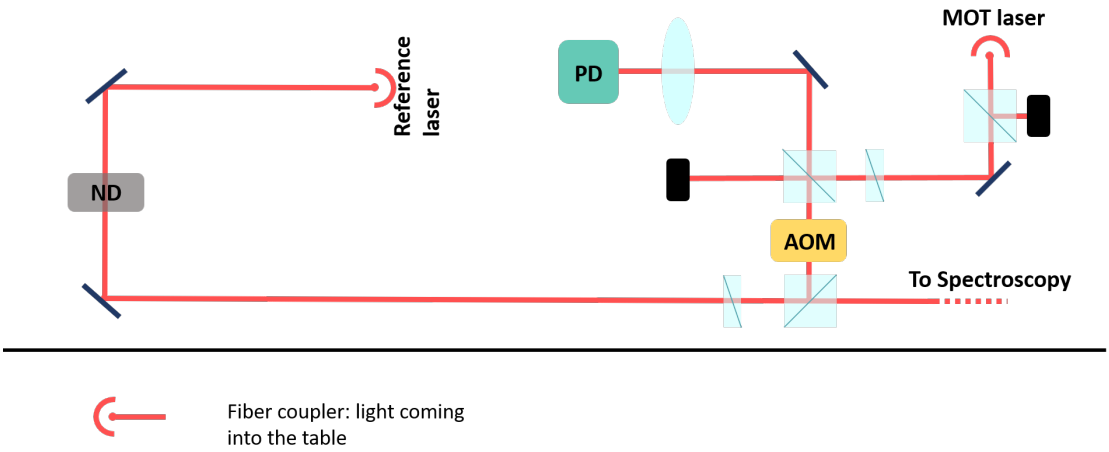

Figure 2.9: Optics setup for frequency offset beat-note locking of the MOT laser to the reference laser.

Then, we combine this modulated reference laser beam with the MOT laser beam. The resultant beam is focused on a photodiode. Let us denote the frequency of the reference laser as f_{main}, the frequency of the un-modulated MOT laser as f_{MOT}, and the AOM frequency as f_{AOM}. Assuming that the main and MOT beams have the same amplitude A, we can write the resultant combined beam as

$$E_{\text{combined}} = A\cos\left(2\pi(f_{\text{MOT}} - f_{\text{AOM}})t\right) + A\cos\left(2\pi f_{\text{main}}t\right). \tag{2.4}$$

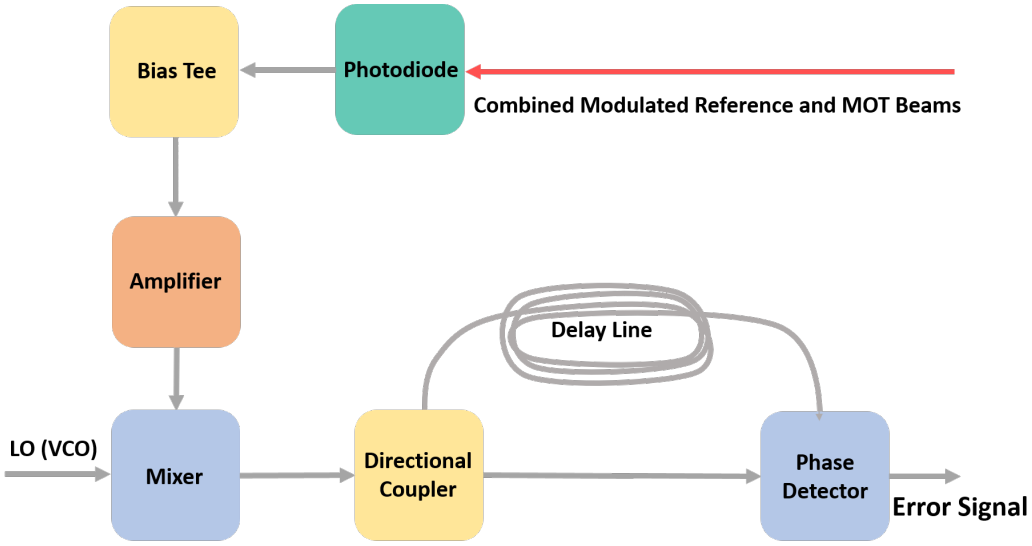

Figure 2.10: Simplified schematic for the electronics setup for frequency offset beat-note locking of the MOT laser to the reference laser. The beam focused on the photodiode is the combination of the modulated reference laser beam and the MOT laser beam (see figure 2.9). A detailed description of the circuit components in our experiment is provided in section 2.3.1.

Using the trigonometric identity for the addition of cosines, the expression can be written as

$$E_{\text{combined}} = 2A \cos\left(\pi(f_{\text{MOT}} + f_{\text{main}} - f_{\text{AOM}})t\right) \cos\left(\pi(f_{\text{MOT}} - f_{\text{main}} + f_{\text{AOM}})t\right).$$

This expression can be thought of as a wave with oscillation frequency $f_{\text{MOT}} + f_{\text{main}} - f_{\text{AOM}}$, with an envelope that oscillates at the smaller frequency $|f_{\text{MOT}} - f_{\text{main}} + f_{\text{AOM}}|$. The envelope frequency is often referred to as the beat note frequency, which we will denote as f_{beat}. Since f_{AOM} and f_{main} have fixed values, changes in f_{beat} reflect changes in f_{MOT}, which is what we would like to set. Therefore, we would like to generate an error signal that would indicate deviations of f_{MOT} from our desired value of it. Additionally, we would like to be able to set

and vary this desired value. To do so, we first separate out the DC component of the signal using a bias tee, then we amplify the oscillatory part of the signal and pass it to a mixer. The mixer receives another signal from a local oscillator (LO) and mixes it with the incoming signal. Similar to the wave addition in equation 2.4, these two signals, after being mixed with each other, would have a frequency component equal to

$$f_{\text{mixer}} = |f_{\text{beat}} - f_{\text{LO}}|.$$

where f_{LO} is the frequency of the local oscillator. To generate the error signal, we scan the frequency of the local oscillator, and split the signal from the mixer into two parts, with one part going through a long coaxial cable (a delay line). The two parts are then sent to a phase detector, which combines the two signals together. The resultant signal is an error signal with a phase that is frequency dependent:

$$V_{\text{Error}} \propto \cos\left(2\pi(f_{\text{LO}} - f_{\text{beat}})\frac{l}{c}\right).$$

where V_{Error} is the error signal, and l is the length of the coaxial cable. The error signal is zero when

$$2\pi(f_{\text{LO}} - f_{\text{beat}})\frac{l}{c} = n\frac{\pi}{2}.$$

We then feed the error signal to a PID controller. To lock to one of the zero crossings of the error signal, the PID controller sends feedback to the MOT laser and adjusts its frequency accordingly. To choose a desired value for f_{MOT}, we can simply adjust f_{LO} which would

result in selecting different values of the zero-crossing lock points on the error signal.

2.3.1 EXPERIMENTAL IMPLEMENTATION

The photodiode beat note signal is first amplified by a Minicircuits ZFL-1200GH+ amplifier, and is then sent to a Minicircuits ZX05-5-S+ frequency mixer. The mixer receives another signal from our local oscillator, a Minicircuits ZX95-850+ voltage controlled oscillator (VCO). The output of the mixer is low-pass filtered through a Minicircuits VLF-1200+, and is then sent to a Minicircuits ZFRSC-2075+ power splitter which splits the signal into two parts. One part of the signal passes through a long coaxial cable (a delay line) and is sent to a Minicircuits ZX05-5-S+ frequency mixer, while the other part of the signal is directly taken to the mixer (no delay line). The output is low-pass filtered through a Minicircuits BLP-1.9+ and is both monitored on an oscilloscope and sent to a PID controller. The PID controller provides feedback for the MOT laser (Toptica TA Pro). A simplified schematic of this circuit is shown in figure 2.10.

3

Beam Box Design and Construction

In this chapter and the next chapter, I will discuss the setup of our experiment, the design processes, and the construction of some of the homemade components.

Our system consists of three main sections: a beam box, an ultra-high vacuum (UHV) system, and lasers and optics. A simplified schematic of the beam box attached to the UHV system is shown in figure 3.1.

The beam box is a cryogenic enclosure which is the site of generation of the cryogenic buffer gas beam (CBGB). The UHV system provides a suitable low-pressure environment for the magneto-optical trap. Lasers and optics are used to produce beams for ablating the potassium target, as well as frequency-locked beams for optical molasses and detection in

the MOT. In this chapter I will focus on the design and construction of the beam box.

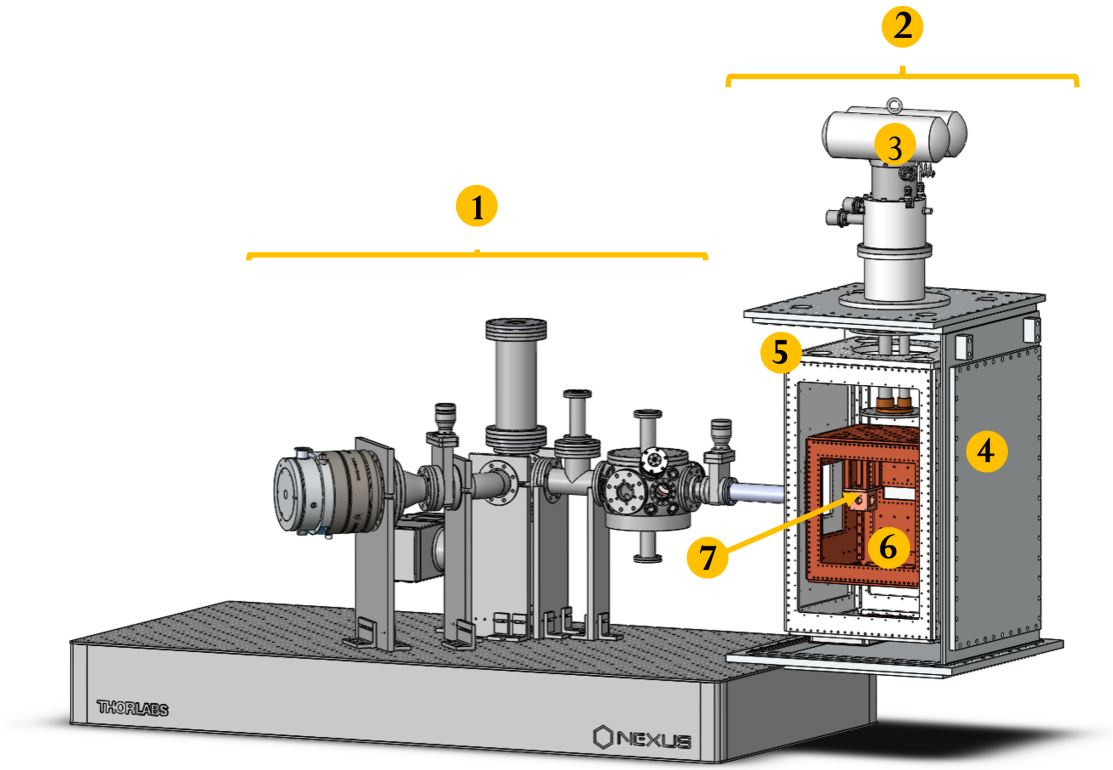

Figure 3.1: Schematic of the beam box connected to the UHV system. 1: UHV system. Details of this portion of the setup are the focus of next chapter. 2: The beam box: site of genereation of the cold buffer gas beam. 3: Pulse tube cryocooler. The schematic is for Cryomech PT415, but our current experiment uses a Cryomech PT410. The beam box design is compatible with both pulse tubes. 4: Room temperature plates (aluminum 6061). 5: 40 K heat shields (aluminum 6061) 6: 4 K heat shields (copper 10100). 7: Buffer gas cell (copper 10100).

3.1 Beam Box

The beam box consists of four major components: a pulse-tube cryocooler, an outer dewar that is vacuum sealed and separates the 300 K room from the inner compartments, two sets of heat shields, and the buffer gas cell housed inside the innermost shield. Each of these components has other accompanying parts and devices that I will describe in the following sections. We use a scroll pump to bring the entire beam box under vacuum. In the innermost compartment, the potassium target is ablated by a pulsed YAG laser beam, and the generated atom cloud thermalizes with cold helium buffer gas, and is then extracted into an atomic beam that leaves the beam box and enters the UHV chamber.

3.1.1 Pulse Tube cryocooler

We use a pulse tube cryocooler from Cryomech (PT410) to cool down the beam box. The PT410 has two cooling stages reaching about 4 K and 45 K. The cooling power of the pulse tube at these stages is 1 W and 40 W, respectively.

Each cooling stage is thermally linked to one set of heat shields using a number of copper braids of diameter ≈ 0.75 inches.

3.1.2 Heat Shields

We have two sets of metal heat shields, one attached to the 4 K stage, and the other attached to the 40 K stage of the pulse tube. These cooled heat shields reduce the radiative heat load that reaches the buffer gas. To maintain the buffer gas cell at a temperature of $\sim$ 4 K, the radiative heat load reaching it should be less than or, at most, equal to the cooling power of the pulse tube, making the heat load reduction provided by the heat shields absolutely

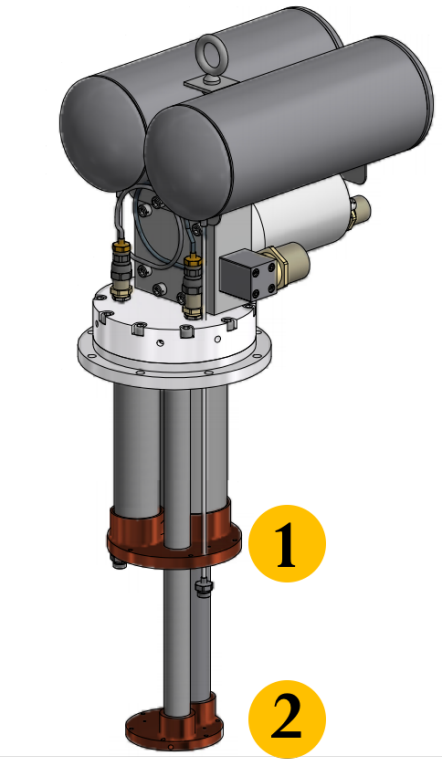

Figure 3.2: Cryomech PT410. 1: 40K cooling stage. 2: 4K cooling stage. Figure taken from Cryomech Website.

necessary, as shown below.

To estimate the radiative heat load, we can look at the temperature differences between the outermost and innermost compartments of the beam box. We should also keep in mind that the radiative heat transfer rate between two surfaces is given by [35]

$$\dot{q}_{\text{rad}} = \sigma A \mathbf{E}(T_2^4 - T_1^4), \tag{3.1}$$

Where σ is the Stefan-Boltzmann constant with value $5.67 \times 10^{-8}\text{W}/(\text{m}^2\text{K}^2)$, A is the area of the smaller surface, and T_1 and T_2 are the temperatures of the colder and warmer

surfaces, respectively [35]. The factor **E** depends on the emissivity and geometry of the surfaces, and for two parallel plates, it is given by [35]

$$\mathbf{E} = \frac{\varepsilon_1 \varepsilon_2}{(\varepsilon_1 + \varepsilon_2 - \varepsilon_2 \varepsilon_2)}.$$

Here, ε_1 and ε_2 are the emissivities of the two surfaces and can be found for various materials in figure 3.9 [35] in the Appendix.

Without the heat shields between the room temperature dewar and the buffer gas cell, we would be dumping about 6 W of power onto the buffer gas cell, which is above the 1W cooling power of the PT410. The T^4 dependence of radiative heat load means that we can significantly decrease the load by using heat shields that are cooled at two stages. Additionally, the 4K shields provide a platform for cyropumping of helium with sorbs [36], the details of which are discussed in section 3.4.

3.1.3 Choice of Materials and Design

The 4 K and 40 K shields in our system are made of copper 10100 and aluminum 6061, respectively. When choosing the material for the heat shields, thermal conductivity, emissivity, weight, and softness/toughness of the material are all factors to consider.

1. **Emissivity:** We can quickly narrow down our choice of materials to metals since they tend to have shiny surfaces and low emissivities, which, based on equation 3.1, makes them suitable for decreasing heat loads [35]. Additionally, all of our surfaces are sanded to 600 grit to further decrease emissivity.

2. **Thermal Conductivity:** Based on fig 3.4, high-purity copper and high-purity aluminum have high thermal conductivities, especially at temperatures between 4 to 20 K.

The high thermal conductivities make the shields easier to cool down when attaching the pulse tube stages to them. The pulse tube stages are only connected to the top of the shields due to geometry constraints. A better thermal conductivity decreases the thermal gradient between the top and bottom of the shields.

3. **Density:** While copper has great thermal conductivity, it also has a very high density that makes it hard to work with. Oxygen-free annealed copper has a density of 8.95 g/cm^3 at room temperature while aluminum 6061 has a density of 2.7 g/cm^3. We use copper for the $4K$ shields, and while the $40K$ shields could also benefit from the high thermal conductivity of copper, they are larger than the $4K$ shields and the system would become extremely heavy if copper were used. As a result, we decided that aluminum was more suitable for the $40K$ shields.

4. **Softness/Toughness:** Copper is a soft element, and screw taps in it can easily get stripped. Screw holes in copper should be helicoiled if they are intended for long term and repetitive use [35]. We use stainless steel helicoils for the 4 K shield. However stainless steel doesn't have great thermal conductivity at cryogenic temperatures and could therefore be limiting when used at thermal joints.

5. **Thermal Expansion/Contraction** Metals tend to contract when temperatures decrease. Consequently, a screw that is joining two metal surfaces will shorten during cooldown cycles. The opposite happens during warmup and the screw lengthens. The metal plates that the screw is joining also go through similar expansion and contraction cycles. If the metal plates and the screws are made from different materials, and if the metal plates contract more than the screw the joint will loosen when temperature is decreased. We can prevent this problem by compensating for the difference in thermal contractions by using a suitable number of stainless-steel washers. Some of the most common materials used in cryogenic constructions are aluminum, brass, copper and stainless steel, in order of decreasing thermal expansion coefficients [35]. One quote from [35] that has come in handy for me numerous times is that "a simple mnemonic to keep this order in mind is to remember your 'ABCs [35]."

3.1.4 Choice of Screws

When choosing screws to join various parts of the shields together, thermal contraction, as well as the force applied by each screw, should be considered.

We use brass screws for both the 40K shield and 4K shields. Both sets of screws are supported by Belville washers have a spring-like structure and are especially useful for joints that will be unscrewed and screwed frequently. Additionally, the 40K screws use a stack of washers to compensate for the difference in thermal contraction of the aluminum plates and the brass screws.

The "ABCs" mnemonic [35] mentioned in section 3.1.3 comes in handy when considering thermal contraction in joints. As an example, if I am joining two copper plates, I would choose brass screws and not stainless steel screws, since brass contracts more than copper, and I would not have to worry about the joint loosening when the system is cooled down. On the other hand, when choosing screws for joining aluminum plates together, we note that both brass and stainless-steel contract less than aluminum and require thermal contraction compensation by washers.

Thermal expansion has a roughly linear behavior for higher temperatures, above room temperature [35]. However, as evident from figure 3.3, thermal expansion is not linear at all for temperatures in the $0 - 100K$ regime. For calculating thermal expansion/extraction at these temperatures, we used reported values from Ekin given in Appendix figure 3.10.

3.1.5 Designing the Heat Shields

When designing the heat shields, it is necessary to keep the total heat load below the cooling capacity of the pulse tube. The total heat load includes radiative heat load from outer,

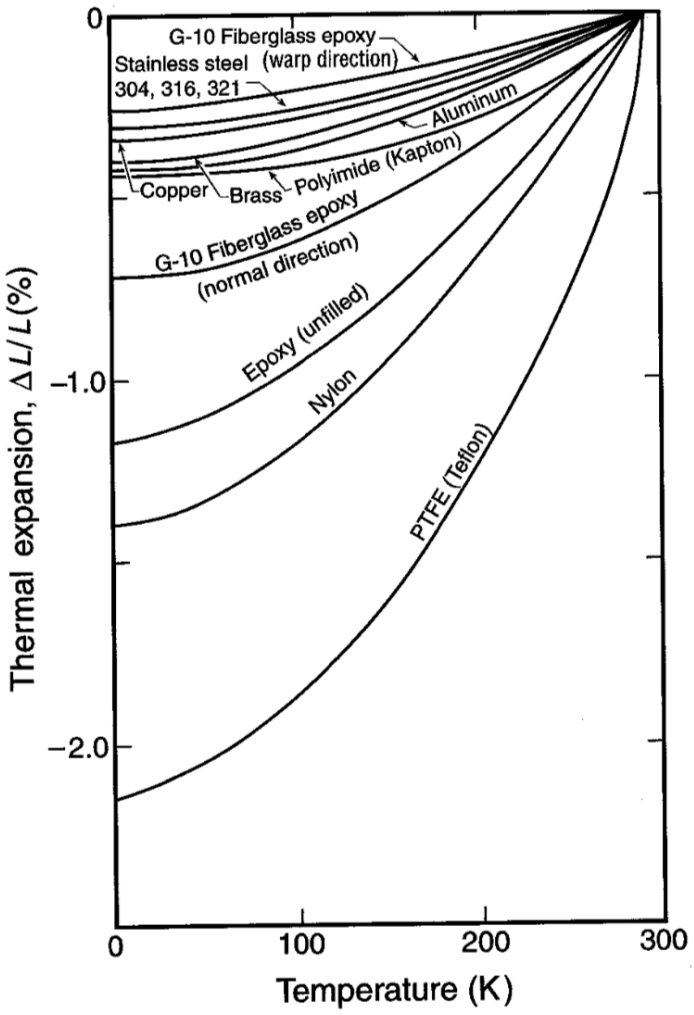

Figure 3.3: Graph of thermal expansion as a function of temperature. Figure taken from section 3.2.2 of Ekin [35]

.

warmer components, and conductive heat load from any attached warm parts. The radiative heat load is given by equation 3.1, and the conductive heat load for an object with con-

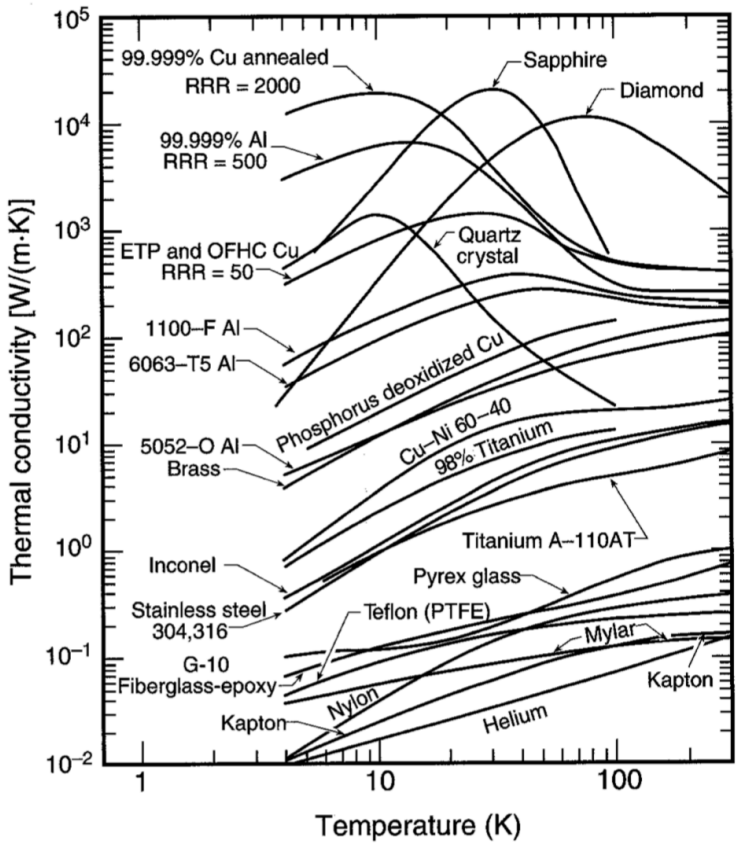

Figure 3.4: Graph of thermal conductivity as a function of temperature for various materials. Figure from Ekin [35]

.

stant cross section can be written as[35]

$$\dot{q}_{rad} = \frac{A}{L}\int_{T_1}^{T_2} \lambda(T)dT. \tag{3.2}$$

Here, A is the cross section, L is the length, and λ is the thermal conductivity [35].

For small temperature differences, we can write the approximate form of the above equa-

tion as

$$\dot{q} = \frac{\lambda A(T_2 - T_1)}{L}. \tag{3.3}$$

3.1.6 Cleaning

Since the beam box is going to operate under vacuum, it is important to clean all surfaces thoroughly. Contaminants stuck on these surfaces will outgas and make it difficult to reach and maintain the desired low pressures. One common evil contaminant that is common for machined parts is machining grease.

We prepare a bath of 2% solution of Citranox in water. We soak the copper parts in the bath for about two to three minutes. We use small brushes to clean any drilled or tapped holes. Afterward, we rinse the copper parts immediately with distilled water followed by an immediate rinse by acetone. We then do a last rinse with isopropanol.

We have noticed that sometimes, if copper parts are left in Citranox for too long, some red, orange, and occasionally brown residues form on the surfaces, which we suspect are the result of Citranox reacting with copper. We are not sure about the process and details of this reaction, but we seem to be able to stop it from happening if we perform the distilled water and acetone rinses immediately after the copper plates are taken out of the Citranox bath.

We soak aluminum or stainless steel parts in a bath of 1% Alconox. We then follow the same procedures as described above, to rinse with distilled water, acetone, and isopropanol.

If we observe persistent contamination on the surfaces, we perform the Alconox/Citranox bath in a sonicator for about ten minutes, and then perform the rinsing steps.

3.2 Super-Insulation Blankets

To reduce the radiation heat load from the outer shields, both 40K and 4K shields are protected with layers of aluminized mylar (superinsulation).

An interesting fact is that superinsulation is also used in spacecrafts to block and reduce radiation [37]. Much of the data and design that we draw on today for cryostat design is, in fact, inspired by research conducted for blocking radiation in spacecrafts.

The idea behind using superinsulation is to stack many thin radiation shields while at the same time avoiding thermal contact between hot and cold layers. The aluminized surface of superinsulation has a low emissivity, which enables it to act as a radiation shield (equation 3.1). Mylar, which is a good insulator, is sandwiched between the two thin layers of aluminum. Mylar, in fact, has a thermal conductivity that is about five orders of magnitude smaller than that of aluminum (figure3.4).

For superinsulation blankets to function properly, pressure must be at most on the order of 10^{-4} Torr; otherwise, conduction by gas molecules will become significant [39]. When installing superinsulation blankets, one should avoid contact between the hotter shields and the superinsulation surfaces, which could create "thermal shorts [38]." Thermal contact plays an important role at lower temperatures, and will become the dominant source of heat transfer at cryogenic temperatures for superinsulation blankets [38]. We can understand this temperature-dependent behavior by noting that while radiation decreases as T^4 (equation 3.1), thermal conduction decreases as T (equation 3.3) and hence dominates at lower temperatures [38].

Because the radiation heat-load from the room temperature shields to the 40K shields is more extreme than the load from the 40K to the 4K shield, we have used typically 16 layers

of superinsulation between the former pair of shields, and typically 8 layers of superinsulation between the latter.

For ease of utility, we folded large sheets of superinsulation into blankets, which are easy to put on and take off from the shields. Each blanket has a set of grommets that can be hung by screws on the individual plates.

(a) (b)

Figure 3.5: (a) Super-insulation blankets covering the 4K shields. We have made cut-outs for the windows. The top surface has various irregularities that do not allow for a blanket. We have simply covered this part with layers of super-insulation. We have used Kapton tape to secure loose ends to prevent thermal shorts. (b) Super-insulation blanket covering one of the 40K shields.

3.3 Buffer Gas Cell

We use a cubic copper cell design previously used in other experiments in the Doyle group. One side of the inner surface of the cell contains a housing for the pressed powder target (our potassium atom source). One of the adjacent faces connects to the the helium fill line, and the face in front of the target has a small window, providing access for the YAG beam which ablates the pressed powder target (see figure 3.6).

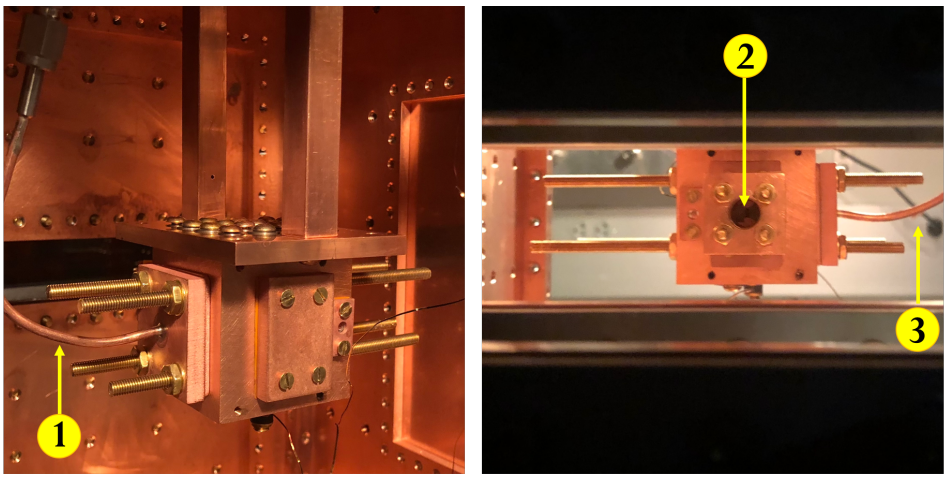

(a) (b)

Figure 3.6: Buffer gas cell cube inside the 4 K shields. (a): The cell is mounted to the top of the 4 K shields using two copper rods. The cold buffer gas beam exits to the right. 1: helium fill line providing the buffer gas. (b): The buffer gas cell cube as viewed through the 40K and 4K windows that provide access for the YAG ablating beam. The viewing angle for this picture is 180 degrees rotated with respect to figure (a). 2: View of pressed powder targets housed inside of the buffer gas cell cube. 3:Helium fill line.

3.3.1 Potassium Pressed Powder Target

We use a pressed powder mixture of KCl and Zr as our potassium source. Zr is added only to add color to the the pressed powder target which would otherwise be almost transparent

and would not be as efficient in absorbing the ablating laser beam.

To make the pressed powder target, we use a hydraulic press to apply 1.4×10^5 KPa to the powder mixture. The resulting pellets are disks of $\sim$ 6 mm in diameter and $\sim$ 0.4 mm in thickness (figure 3.7).

Even though the KCl powder contains other isotopes of potassium beside ^{39}K, it can serve as a reliable source of ^{39}K, since ^{39}K has a natural abundance of 93.2581%.

(a) (b)

Figure 3.7: (a) Pressed powder potassium targets. The transparent/white-appearing target is pure KCl while the black target contains small amounts of Zr. (b) Both targets mounted on the target holder. We use Stycast 2850 to attach them to the copper surface. The transparent target also appears black due to Stycast.

3.4 Sorbs

Since we use helium as our buffer gas, we need to remove residual helium to avoid its buildup that could raise the pressure inside the beam box. One method that the Doyle Lab commonly uses for removing residual helium is installation of charcoal "sorbs."

Charcoal acts by "cryopumping" helium. During this process gas molecules freeze onto the cold charcoal surface and start diffusing to the inner parts of the charcoal grain [40]. Charcoal is extremely porous, which provides a large surface area of about 1000 m^2/g for

cryopumping [42]. It is the continuous diffusion of helium atoms to the core of the charcoal grain that allows continuous cryopumping. There are two situations in which cryopumping no longer works, or loses efficiency. One situation is when nearly all available volume for charcoal has been used up [42]. In such a situation, it is possible to warm up the sorbs and allow for the helium atoms to diffuse out of the charcoal grains while simultaneously pumping on the beam box to remove the old helium [42]. Sorbs are about seven orders of magnitude more efficient in pumping helium than scroll pumps, and that's why they are necessary.

As previous experiments by other members of the group have shown, another situation where the sorbs stop cryopumping is when the diffusion of the helium atoms to the core of charcoal grains stops due to cold temperatures at about $2 - 3$K [42].

3.4.1 Construction of the sorbs

We use coconut charcoal with US mesh size of 12×30, which has been shown to have the best pumping characteristics among the many tested cryopump materials [40]. We machined ten 5.4×2.6 inch plates of thickness 0.063 inch to use as base plates for the coconut charcoal. Two of these plates have extra holes for mounting thermometers to them.

We mount these plates in a stacked fashion at the inside surface of the bottom $4K$ shield plate. The stacking of the sorbs reduces the probability of contamination for the innermost sorb plates since these outer sorbs provide both a physical barrier for potential contaminants and also cold cryopumped surfaces that reduce the chances of any already-existing contaminants hovering in the area [36]. Both references [36, 42] provide detailed outlines of the procedure for making these charcoal sorbs. I also outline the steps that we follow

here:

1. **Cleaning the plates:** Since these plates will be under vacuum it is necessary to clean them. We use the copper cleaning procedure outlined in section 3.1.6.

2. **Kapton masking:** We apply Kapton tape to the parts of the surface that will not be covered with charcoal. Some of these surfaces might include attachment areas for mounts and thermometers.

3. **Preparing the surface:** We use a moderately rough sandpaper (100 or 400 grit) to make the surface of the copper a little rough. This will enhance the bonding of Stycast to the surfaces, which is used to bind charcoal to the copper.

4. **Stycasting:** We use Stycast 2850 mixed with catalyst 24LV to cover the surfaces of the copper plates. Note that the Stycast should cover the entire surface, but it should be applied in a thin layer to allow for better thermal contact. This Stycast mixture doesn't have the best thermal conductivity among possible binding materials [40], however, it forms a strong and durable bond since its thermal expansion coefficient is similar to that of copper [40].

5. **Covering with charcoal:** We sprinkle charcoal to cover all Stycasted surfaces. It is important to let the charcoal grains settle under gravity only, and to avoid using extra force.

6. **Storage:** After the Stycast has settled, we store the sorbs in plastic bags to prevent contamination.

3.5 Windows

We have two windows on each sets of shields, as well as two windows on the room temperature plates. These windows provide access for the YAG ablation beam, and for in cell absorption spectroscopy.

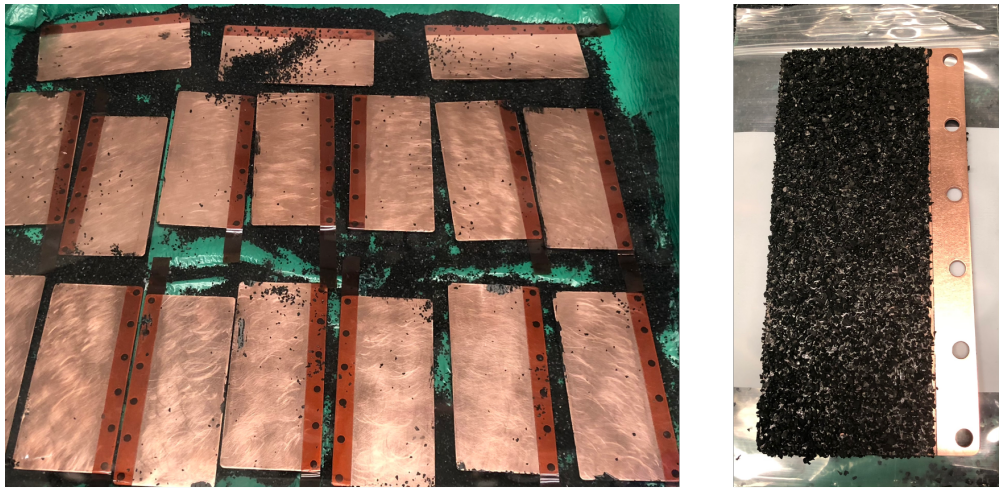

(a) (b)

Figure 3.8: (A) Sorb plates before application of Stycast. We have covered the areas that are going to be used for mounting with Kapton tape, and have sanded the surface of the plates. (b) A prepared sorb after Stycasting and sprinkling of charcoal.

The four inner windows are 1.75×5.75 in, and they have a thickness of $3/8$ in. The outer window is 7×2 in and 0.75in thick. All windows are made of borosilicate glass.

To mount the windows, we apply Kapton tape on the shield plates, around the window openings. These tapes serve as cushions for the windows and lower their probability of cracking. Then, the glass is put on the appropriate location and is mounted using a Kapton-covered flange that screws onto the corresponding plate.

The outer window needs to be vacuum sealed. We use a Viton o-ring that sits inside an o-ring groove on the room-temperature plates. Data and instructions for designing an o-ring groove, and choosing the correct size of Viton o-rings, is provided in the Parker O-ring Handbook [41].

3.5.1 Thermometers

We use silicon diode thermometers by LakeShore to monitor temperatures of various parts of the heat shields, the buffer gas cell, and sorbs during cooldown and warmup cycles. These thermometers have extremely thin wires, and care should be taken when handling them. The thermometer signal goes to a LakeShore Model 218 temperature reader, and is transferred to our LabView monitoring software.

We use a 41-pin feedthrough by Kurt J. Lesker for our thermometer wires.

Material	Emissivity		
	Polished	Highly oxidized	Common condition
Metallic			
Ag	0.01		
Cu	0.02	0.6	
Au	0.02		
Al	0.03	0.3	
Brass	0.03	0.6	
Soft-solder			0.03
Nb, crystalline, bulk			0.04
Lead	0.05		
Ta	0.06		
Ni	0.06		
Cr	0.07		
Stainless steel			0.07
Ti			0.09
Tin (gray), single crystal			0.6
Nonmetallic			
IMI 7031 varnish			0.9
Phenolic lacquer			0.9
Plastic tape			0.9
Glass			0.9

Sources:

American Institute of Physics Handbook (1972), 3rd edition, Chapter 6, McGraw-Hill, New York.

M. M. Fulk, M. M. Reynolds, and O. E. Park (1955), *Proc. 1954 Cryogenic Eng. Conf.*, Nat. Bur. Stands. (US) Report No. 3517, p. 151. US Government Printing Office, Washington, DC.

W. H. McAdams (1954), *Heat Transmission*, 3rd edition, McGraw-Hill, New York.

W. T. Ziegler and H. Cheung (1957), *Proc. 1956 Cryogenic Engineering Conference*, National Bureau of Standards, p. 100. US Government Printing Office, Washington, DC.

Emissivities of additional materials at room temperature are available in the technical reference section of *The Temperature Handbook* (2002), p. Z-171. Omega Engineering Inc., Stamford, CT (http://www.omega.com/).

Figure 3.9: Table of emissivities for various materials [35].

Thermal expansion/contraction of technical materials

Material	$\Delta L/L$ at 4 K [%]	$\Delta L/L$ at 40 K [%]	$\Delta L/L$ at 77 K [%]	$\Delta L/L$ at 100 K [%]	$\Delta L/L$ at 150 K [%]	$\Delta L/L$ at 200 K [%]	$\Delta L/L$ at 250 K [%]	α at 293 K [10^{-6} K^{-1}]
Metals								
Ag [b]	0.413	0.405	0.370	0.339	0.259	0.173	0.082	18.5 [h]
Al [a]	0.415	0.413	0.393	0.370	0.295	0.201	0.097	23.1 [b]
Au [b]	0.324	0.313	0.281	0.256	0.195	0.129	0.061	14.1
Be [b]	0.131	0.131	0.130	0.128	0.115	0.087	0.045	11.3 [d]
Cu [a]	0.324	0.322	0.302	0.282	0.221	0.148	0.070	16.7 [i]
Fe [a]	0.198	0.197	0.190	0.181	0.148	0.102	0.049	11.6 [b]
Hg [b,*]	0.843	0.788	0.788	0.592	0.396	0.176	*	57.2 *
In [b]	0.706	0.676	0.602	0.549	0.421	0.282	0.135	32.0
Mo [b]	0.095	0.094	0.090	0.084	0.067	0.046	0.022	4.8 [d]
Nb [a]	0.143	0.141	0.130	0.121	0.094	0.063	0.030	7.3 [d]
Ni [a]	0.224	0.223	0.212	0.201	0.162	0.111	0.053	13.4 [d]
Pb [b]	0.708	0.667	0.578	0.528	0.398	0.263	0.124	29
Ta [b]	0.143	0.141	0.128	0.117	0.089	0.059	0.028	6.6
Sn [b] (white) [r]	0.447	0.433	0.389	0.356	0.272	0.183	0.086	20.5
Ti [a]	0.151	0.150	0.143	0.134	0.107	0.073	0.035	8.3 [b]
W [b]	0.086	0.085	0.080	0.075	0.059	0.040	0.019	4.5
Alloys								
Al-6061-T6 [c]	0.414	0.412	0.389	0.365	0.295	0.203	0.097	22.5
Brass (65%Cu–35%Zn) [b] (yellow brass)	0.384	0.380	0.353	0.326	0.253	0.169	0.080	19.1 [b]
Constantan (50%Cu–50%Ni) [b]	—	0.264	0.249	0.232	0.183	0.124	0.043	13.8 [b]

Definitions: $\Delta L/L \equiv (L_{293\,K} - L_T)/L_{293\,K}$; $\alpha \equiv (1/L)\, dL/dT$.

Figure 3.10: This is a section of a table from Ekin [35]. Note that I have included only one section of the table. Please refer to section A:6.4 of the referenced Ekin edition for the complete table.

4

Optics Setup and Experiment Sequence

In this chapter, we will describe the setup for the MOT optics and 1D transverse Doppler cooling, as well as the experiment control sequence.

4.1 MOT Optics

In section 1.2.3, we discussed the significance of repump and cooling lasers. The frequencies of these two beams and their relation to the potassium electronic structure is shown in figure 4.2. In order to obtain these frequencies from the MOT laser, the MOT laser beam that is offset-locked to the reference is split into a repump and a cooling branch. The repump and cooling branch beams pass through AOMs that shift their frequencies

by +129.9 MHz and −336.9 MHz, respectively. These branches are then recombined and further split into two branches to get the vertical and horizontal MOT beams, each with 110 mW of power (see figure 4.1). The various modulations on the reference laser and the MOT laser to get the repump and cooling lights with respect to the lock points are shown in figure 4.3.

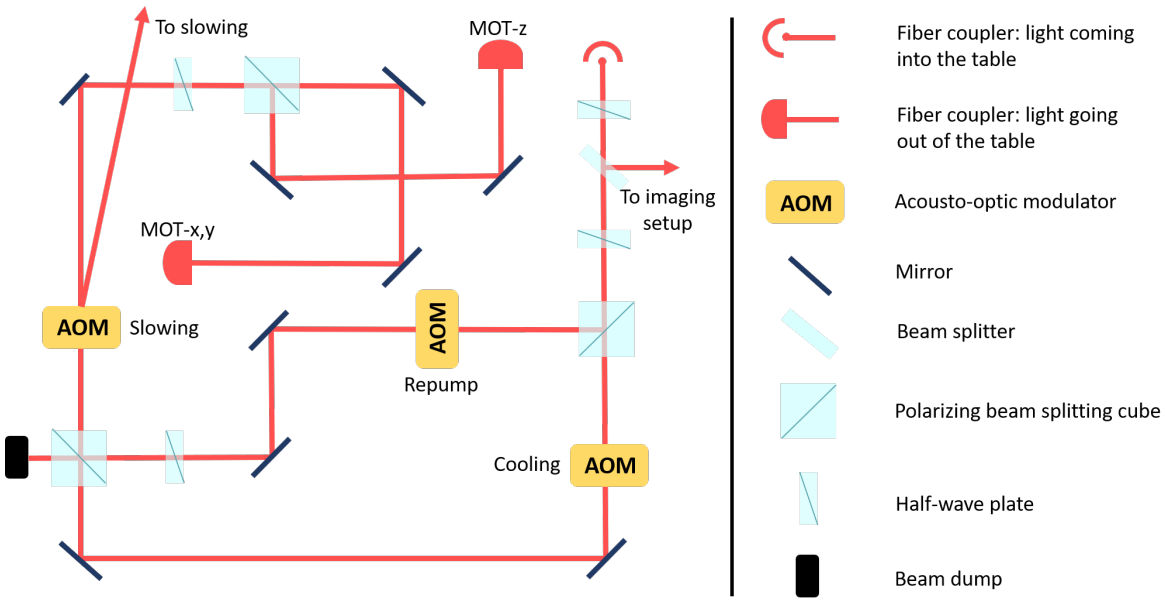

Figure 4.1: Setup for obtaining the MOT beams. The MOT laser beam is split into two branches and modulated by two AOMs to obtain repump and cooling beams. The beams are then recombined and sent to another AOM for chirped slowing. The zeroth order of the beam passing through this AOM is not modulated and is split into two branches to obtain the horizontal and vertical MOT beams. The −1st order of the beam passing through the slowing AOM is used for chirped slowing.

4.2 Chirped Slowing

In order to sweep the frequency of our MOT laser for chirped slowing, we program a Rigol arbitrary waveform generator to sweep the frequency of the beat note lock set point from 262 MHz to ∼ 445 MHz in 1 ms.

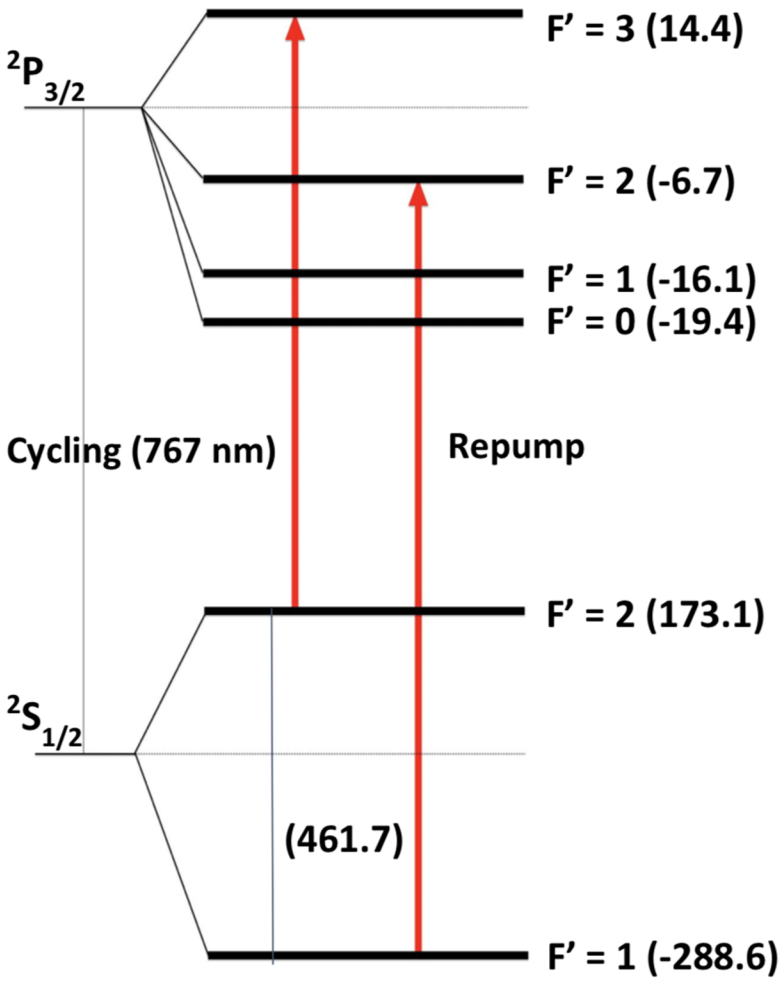

Figure 4.2: Cycling and repump transitions of ^{39}K.

In order to get the chirped slowing light, the combined cooling and repump beams pass through an AOM with a frequency shift of -57MHz. When the AOM is on, we take the -1st order beam for chirped slowing. The zeroth order beam goes directly to the vertical and horizontal MOT beams (see figure 4.1). We send the chirped slowing beam down the potassium beam propagation axis.

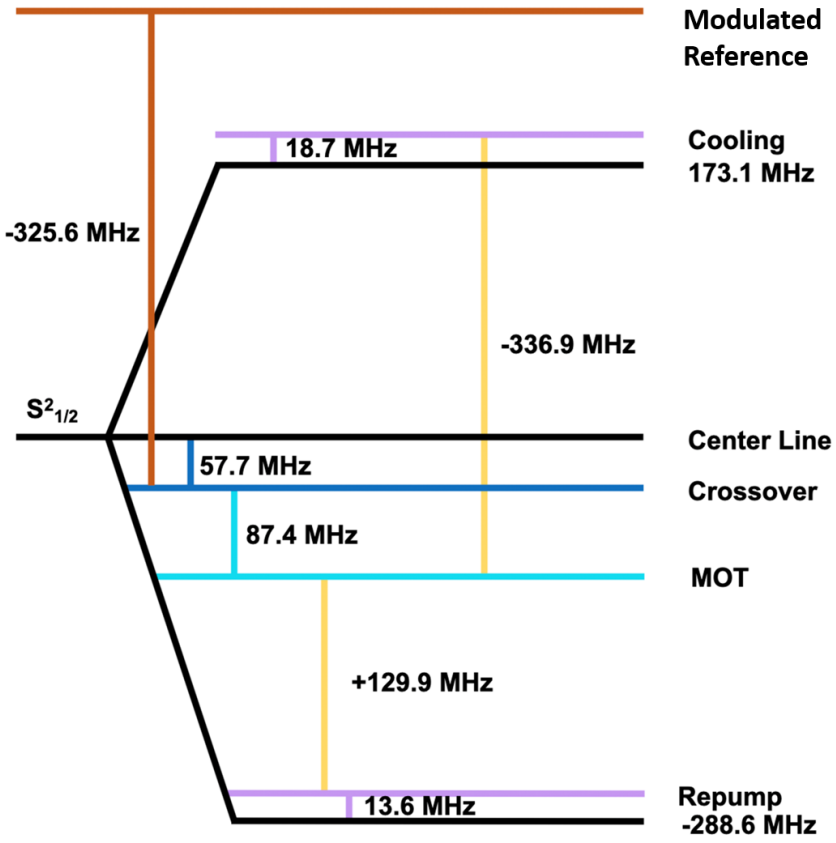

Figure 4.3: Different frequency references in the experiment. The crossover is where the reference laser is locked to. Modulated reference refers to the frequency of the reference laser after passing through the AOM in figure 2.9. The MOT light is frequency offset locked to the modulated reference. The cooling and repump lights are obtained from modulating the MOT light as discussed in section 4.1.

4.3 1D Transverse Doppler Cooling

We implement a 1D transverse Doppler cooling method, perpendicular to the potassium beam propagation axis. Ideally, cooling in this direction should lead to a collimation of the beam in the cooling direction. We use a Ti:Sapphire laser and generate a beam with 1:6 ratio of repump to cooling light. We split this beam into two arms using a fiber split-

ter. We expand each arm by 2x using cylindrical lenses (final Gaussian beam 1/e radius is 2mm x 4mm). We then send these beams in opposite directions through the beambox windows (figure 4.4). Each beam has as power of 120 mW and an optimized red detuning of 14 MHz.

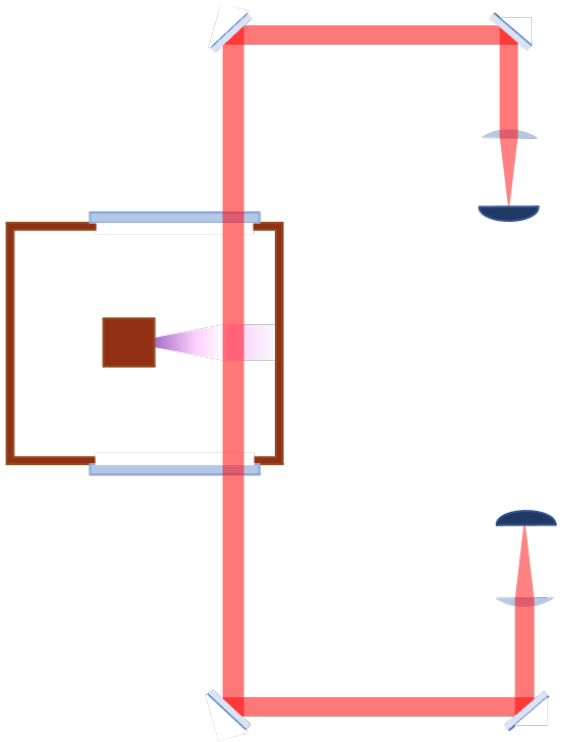

Figure 4.4: Simplified schematic of 1D transverse Doppler cooling beams and their relation to the potassium atomic beam (purple). We obtain the two separate beams by using a fiber splitter. For simplicity, the 40K and room temperature shields are not shown. The beams are set up outside the beam box and travel through the windows of all beambox shields.

4.4 Experiment Timing

The timing of various events during the experiment is shown in figure 4.5. The frequency ramping sequence for chirped slowing is shown in figure 4.6.

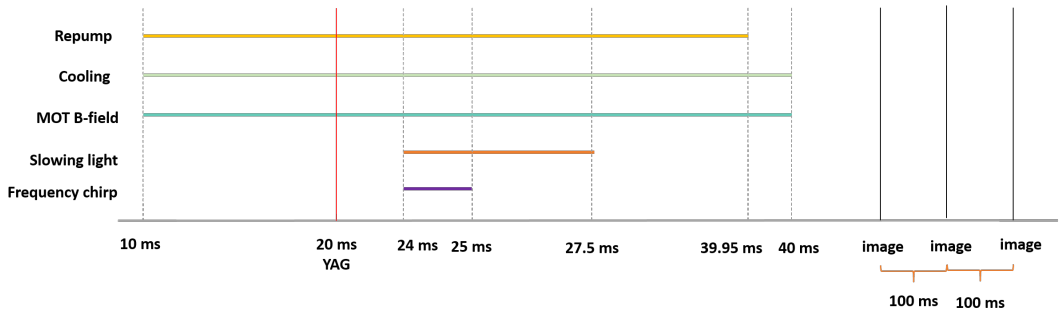

Figure 4.5: Timing of experiment events. Note that time intervals are not drawn to scale. The first imaging begins at a variable time after the MOT B-field and the cooling lights turn off. The imaging pulses are separated by 100 ms and each lasts for 30 μs.

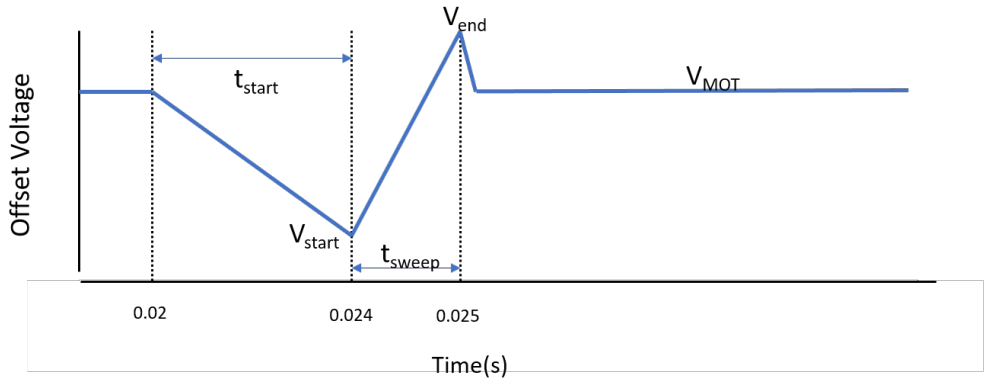

Figure 4.6: Timing of the chirped slowing events. The slowing happens during the 1ms of frequency ramping denoted by t_{sweep}. V_{start}, V_{end}, and V_{MOT} correspond to 262MHz, 445MHz, and 416 MHz for the beat note frequency respectively.

5

MOT Characterization and Results

To characterize a MOT, we would like to know the total number and density of trapped atoms, the loading rate, lifetime, and temperature of the MOT. In this chapter we will discuss the methods used to measure and calculate these MOT characteristics.

5.1 Atom Number and Density

To determine the total number and the density of the atoms trapped in the MOT, we use absorption imaging. In this imaging method, an imaging beam is sent down one of the optical ports on the MOT chamber. The beam interacts with the trapped atoms inside the chamber and gets absorbed to cause a transition, in our case, the repump transition

(section 1.2.3). As a result, the intensity of the beam after passing through the trap is lower and could be used as a measure to determine the density of the atoms. The outgoing beam is focused on a charge-coupled device (CCD) camera. The intensity of a beam that is on resonance, after it passes through the trap and experiences absorption, is given by Beer's law [43]:

$$I_f = I_0 e^{-\sigma_0 n}, \tag{5.1}$$

where I_0 is the initial beam intensity, I_f is the final beam intensity after passing through the atoms, $\sigma_0 = 3\lambda^2/(2\pi)$ is the absorption cross section, and $n = \int_{-\infty}^{\infty} \rho(x, y, z) dz$ [43, 44] is the atom number density in the propagation direction z. For these measurements we are assuming that $I_0 \ll I_{sat}$.

The optical density (OD) is generally defined as [43]:

$$\mathrm{OD} = \ln \frac{I_0}{I_f}. \tag{5.2}$$

Rearranging equation 5.1, taking the natural logarithm of both sides, and using equation 5.2 yields

$$n = \frac{\mathrm{OD}}{\sigma_0}. \tag{5.3}$$

When measuring this OD in experiment however, we need to subtract background noise and scatter. To do so, we take three images on the CCD: 1- image with the imaging beam and the MOT both being on (I_{atoms}) 2- image with MOT being off and imaging beam be-

ing on (I_{beam}). 3- background image with both MOT and imaging beam being off (I_{dark}). To account for the background, the OD then becomes

$$\text{OD} = \ln \frac{I_{\text{beam}} - I_{\text{dark}}}{I_{\text{atoms}} - I_{\text{dark}}}. \tag{5.4}$$

This version of the OD (equation5.4) is what we use in equation 5.3 to get the atom number density.

Experimentally, n corresponds to the number density of atoms inside a column with a camera pixel as its base [43]. We can then calculate the total number of atoms in the MOT by summing the number of atoms over all the pixels in the imaging field [43]. We also need to consider the linear demagnification (d) which represents the ratio of the length of a pixel to the length of the real physical area that it images. For our experiment, $d = 1/3$. More details on how to calculate the demagnification of a system can be found in [45].

We can write the total number of atoms N as

$$N = \frac{1}{d^2} \sum_{i=1}^{m} n_i \, A = \frac{1}{d^2} \sum_{i=1}^{m} \frac{\text{OD}_i}{\sigma_0}, \tag{5.5}$$

where A is the pixel area which is $(5.6\ \mu\text{m})^2$ for our camera, and m is the total number of pixels.

To calculate the density of the MOT, we first perform a 2D Gaussian fit on the absorption images and use the $1/\sqrt{e}$ radius (1 σ radius) in the x and y directions as measures for the size of the MOT. We then approximate the volume of the cloud based on these dimensions. The density is then estimated by dividing the total number of atoms from equation

5.5 by the volume

$$\rho = \frac{N}{(2\pi)^{3/2}\sigma_x^2\sigma_y},$$

where σ_x is the size along the imaging direction.

5.1.1 Atom number and density measurements

We took absorption images of our buffer gas-loaded MOT on a Guppy Pro (CCD camera). We analyzed these images in MATLAB and Python. To get the total atom number we performed calculations based on equation 5.5 on 251 images from an optimized MOT. The averaged result of these calculations indicates a buffer gas-loaded MOT with total atom number of

$$\boxed{7.2 \times 10^7 \text{ atoms}}$$

and density of

$$\boxed{1.5 \times 10^{10} \text{ atoms/cc}}$$

The averaged image used to calculate these numbers is shown in figure 5.1. This particular measurement was taken with the beam undergoing chirped slowing, as well as 1D Doppler cooling. The chirped slowing in this case lasted for 1 ms and the MOT beams were offset-locked by 416 MHz to the reference laser.

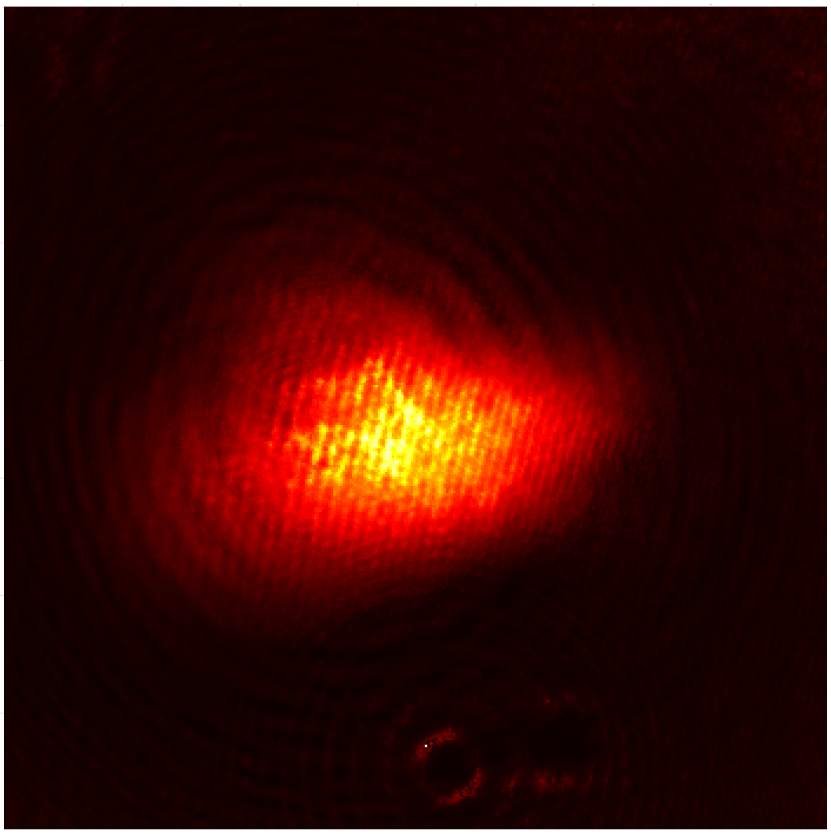

Figure 5.1: Averaged OD image of our buffer gas loaded potassium MOT over 251 images. The averaged result indicates a total atom number of 7.2×10^7 and a density of 1.5×10^{10} atoms/cc. 2D Gaussian fitting to the above image yields $1/\sqrt{e}$ dimensions of 0.8 mm and 0.49 mm in the x and y directions, respectively.

5.2 MOT Temperature

We use time of flight (TOF) measurements to determine the temperature of the MOT. In these measurements, we assume that the atoms inside the MOT do not interact with each other and that they follow a Maxwell-Boltzmann thermal distribution [45]. As a result, once the MOT is turned off, the atomic cloud expands consistent with classical thermal motion of each atom [45]. By taking successive images during this expansion, we can mea-

sure how fast the the expansion occurs and deduce the cloud's temperature.

To derive this temperature quantitatively, we first note that the one dimensional velocity distribution of the atoms in the cloud is given by the Maxwell-Boltzmann distribution:

$$p(v)dv = \left(\frac{m}{2k_{\mathrm{B}}T}\right)^{1/2} e^{-\frac{mv^2}{2k_{\mathrm{B}}T}} dv, \tag{5.6}$$

where k_{B} is the Boltzmann constant, m is the mass of the atoms, and T is the temperature of the cloud. Assuming that the cloud starts out as a point, we can write the simple kinematics relation $v = \frac{x}{t}$ [45]. Substituting for velocity in equation 5.6, and performing a change of variables, we can write

$$p(x,t) \propto e^{-\frac{mx^2}{2k_{\mathrm{B}}Tt^2}} dx. \tag{5.7}$$

We can match this Gaussian function to the form of a standard Gaussian probability distribution[45]:

$$f(x) = \frac{1}{\sigma\sqrt{2\pi}} e^{\frac{-x^2}{2\sigma^2}}.$$

Hence, we see that equation 5.7 has variance [45]

$$\sigma^2(t) = \frac{k_B T t^2}{m}.$$

We can use σ as a measure of the size of the atomic cloud at time t. In reality, the cloud size

at zero is not zero, hence we would need to account for the initial size σ_0 [45]:

$$\sigma^2(t) = \frac{k_B T t^2}{m} + \sigma_0^2 \tag{5.8}$$

Experimentally, we image the atomic cloud at multiple time-points, and measure its size in one dimension. We can then use equation 5.8 to determine T which is the temperature of the cloud. We should note that in equation 5.8, we are using the real physical dimensions of the atomic cloud which we need to obtain from the measured dimensions in pixels [45]:

$$\sigma(t) = \frac{s(t) l_{\text{pixel}}}{d},$$
$$\sigma_0 = \frac{s_0 l_{\text{pixel}}}{d},$$

where s_0 and $s(t)$ are the dimension of the cloud at times 0 and t, measured in pixels. Variable d is the demagnification of the system, and l_{pixel} is the length of each pixel.

5.2.1 Measurement and analysis

We imaged a buffer gas-loaded MOT at varying times after the loading start time. The averaged dimensions of about 60 images for each of the imaging times were used to calculate temperature in the x and y directions by fitting the data to equation 5.8. These fits are

shown in figure 5.2. These measurements indicate a temperatures of

$$\boxed{13.4 \text{ mK in the horizontal direction}}$$

and

$$\boxed{4.9 \text{ mK in the veritcal direction}}$$

The observed imbalance in temperature in the two directions is likely due to imbalanced powers of the cooling and repump as well as imbalanced overall power in the z versus x and y beams. These factors could be further improved in later iterations of the experiment.

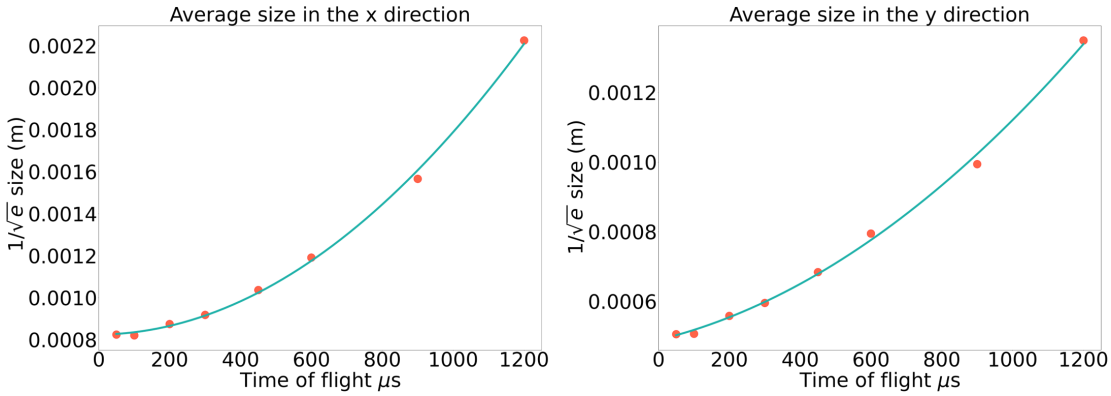

Figure 5.2: Time of flight measurements and fit. Absorption images of the MOT taken at various times after loading the MOT. The dimensions were estimated using 2D Gaussian fits. The cloud expansion over time in the horizontal and vertical directions is fit to equation 5.8, and yields temperatures of 4.9 mK and 13.4 mK in the horizontal and vertical directions, respectively.

5.3 MOT LOADING RATE

To understand how the number of atoms in the MOT changes, we need to consider the rate at which the atoms are "loaded" into the MOT, as well as the rate at which they are lost from it. In general, we can write the rate equation for a MOT as [46]

$$\frac{dN}{dt} = R(t) - \gamma N(t) - \beta(N(t))^2. \tag{5.9}$$

Where $N(t)$ is the number of atoms in the trap. We define each of the terms in the rate equation below.

$R(t)$ is the loading rate of the atoms into the trap. For atoms to get trapped in the MOT, they must have a velocity below the capture velocity v_c. We can derive a simple expression for the capture velocity by considering the kinematics of the atoms. From equation 1.16, we can see that the maximum force the MOT can apply to an atom is $\hbar k\Gamma/2$. Consider the kinematics relation $v_{\text{final}}^2 - v_{\text{initial}}^2 = 2ad$, for a being the acceleration of the object, and d being the distance over which it travels. The maximum velocity that can be brought to zero under the influence of the maximum scattering force over the diameter D of the MOT beam is then given by

$$v_c = \sqrt{\frac{\hbar k \Gamma D}{m}}. \tag{5.10}$$

The capture velocity of our potassium MOT is about 80 m/s.

$\gamma N(t)$ is the loss rate of the atoms due to them colliding with the background gas [46]. We will refer to γ as the background collision loss rate coefficient.

$\beta(N(t))^2$is the loss rate due to two atoms colliding with each other [46] and is referred to as the two-body loss rate. We consider this term to be negligible for our MOT because our densities are not large enough. Hence the rate equation becomes

$$\frac{dN}{dt} = R(t) - \gamma N(t)\cdot \tag{5.11}$$

For a buffer-gas loaded MOT however, the loading rate is not constant. The dynamics of a buffer gas-loaded MOT have been extensively discussed in [9]. They indicate that the loading rate for such a MOT can be approximated as a Gaussian pulse [9]:

$$R(t) = \frac{n_{\text{tot}}}{w\sqrt{2\pi}} e^{-\frac{(t-t_0)^2}{2w^2}}, \tag{5.12}$$

with t_0 defined as the time that the pulse arrives at the MOT region, w defined as the width of the pulse, and $n_{\text{tot}} = \int_{-\infty}^{\infty} R(t)dt$ [9].

Solving equation 5.11 with this pulsed loading rate gives [9]

$$n(t) = \frac{n_{\text{tot}}}{2} e^{\frac{1}{2}}\gamma(-2(t-t_0) + \gamma w^2)\cdot \tag{5.13}$$
$$\left(\text{erf}\left(\frac{t_0 + \gamma w^2}{w\sqrt{2}}\right) - \text{erf}\left(\frac{-t + t_0 + \gamma w^2}{w\sqrt{2}}\right)\right),$$

where $\text{erf}(x) = \frac{2}{\sqrt{\pi}} \int_0^x e^{-t^2} dt$ [9].

5.3.1 Measurement

We have measured the loading rate of our MOT when it is loaded from a dispenser that sits at one of the ports of the MOT chamber. We loaded the MOT and took absorption images

after varying amounts of time. Then we performed a fit to determine γ and $N_{\max}$. Based on these two numbers, we calculated R. Our measurements indicate $N_{\max}$ of about 7×10^6 atoms and γ of 0.68s^{-1}. These values give us a loading rate R of 4.8×10^6 atoms/sec for a dispenser-loaded MOT.

We also measured the dynamics of a buffer gas-loaded MOT by looking at the fluorescence of the MOT on a photomultiplier tube (PMT). We fit the averaged trace to equation 5.13 to estimate γ and w. We obtained fit parameters of $w = 4.63$ ms, and $\gamma = 23.83\ \text{s}^{-1}$, indicating a $1/\gamma$ lifetime of 41.97 ms.

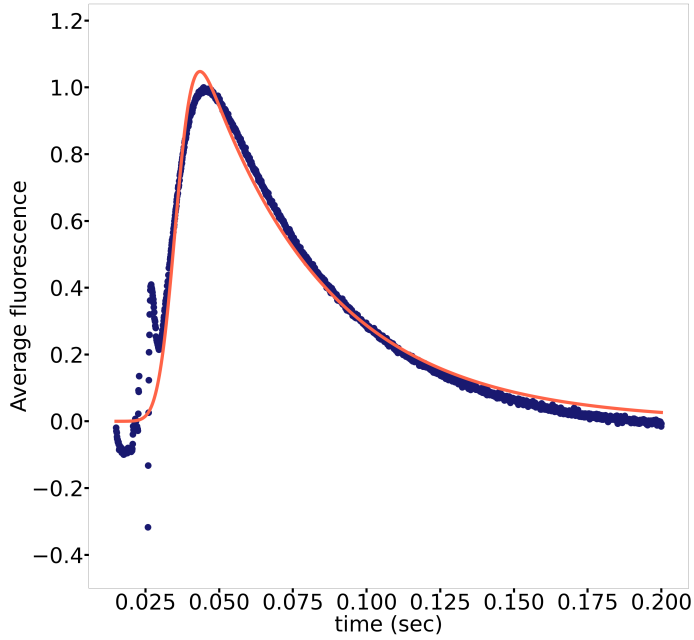

Figure 5.3: Averaged fluorescence data and fit of a buffer gas-loaded MOT as measured on a PMT. The y-axis is measured in arbitrary units and is normalized to the peak fluorescence. The pink line indicates a fit to equation 5.13. We obtained fit parameters of $w = 4.63$ ms, and $\gamma = 23.83\ \text{s}^{-1}$, indicating a $1/\gamma$ lifetime of 41.97 ms.

6

Outlook

We have been able to demonstrate a buffer gas loaded MOT of potassium atoms with the high density of 1.5×10^{10} atoms/cc in a timescale of order 10 ms. Previous work on atomic MOTs, which are loaded either from dispenser or oven sources does not achieve sub-100ms loading rates. Our buffer gas loaded dense MOT provides a platform for experiments that require fast MOT loading times or high repetition rates.

Additionally, our experiment provides an ideal starting point for evaporative cooling and eventual quantum simulation applications in optical tweezers or lattices.

We have implemented a number of recent improvements to our experiment. We have decreased the beam exit aperture size on the 40K front shield from 6.35 cm in diameter

to 2 cm in diameter and have also added a shutter in the beam exit aperture on the room temperature shields. These modifications have decreased our MOT background pressure and increased the MOT lifetime from 41.97 ms to $\sim$ 140ms.

We have also added a Zeeman slower to the setup which has increased the total number of trapped atoms to 150 million, which is about 5$\times$ higher than the number trapped with only chirped slowing (no 1D Doppler cooling).

We attempted to implement a 2D Doppler cooling setup inside the beam box, however, we have not been able to see improved results yet, potentially due to difficulties and imperfections in alignment.

Further improvements we have implemented include increasing the MOT beam sizes and balancing the beam intensities better. These modifications have led to smaller temperatures and higher densities.

Future potential improvements to the current setup include balancing the repump and cooling power in the MOT beams and improving alignment of the 2D Doppler cooling.

These future modifications would aim to increase the atom number and the corresponding density by at least an order of magnitude. As mentioned before, we have demonstrated a technique of loading a MOT from a CBGB that offers a way of loading a high-number, dense MOT faster than is achievable with other previously demonstrated methods. This method could improve experimental cycle times by one or two orders of magnitude. Additionally, our technique opens up possibilities for trapping atoms with high melting points, such as chromium with a melting point of 3500 F, that are difficult to produce in ovens.

References

[1] Gross, Andreas J, Herrmann, Thomas R. W. (2007). History of lasers. World Journal of Urology, 25(3), 217-220.

[2] Phillips, W. D. (1998). Nobel Lecture: Laser cooling and trapping of neutral atoms. Reviews of Modern Physics, 70(3), 721-741.

[3] Bohigas, J., An analytical model for the evolution of the coldest component of the Boomerang Nebula, Monthly Notices of the Royal Astronomical Society, Volume 466, Issue 2, April 2017, Pages 1412–1420, https://doi.org/10.1093/mnras/stw3187

[4] Fixsen, D.J., 2009. The temperature of the cosmic microwave background. The Astrophysical Journal, 707(2), p.916.

[5] Schwartz, M. Harvard Physics 181 Lecture Notes on BEC, (2020).

[6] Anderson, Mike H., et al. "Observation of Bose-Einstein condensation in a dilute atomic vapor." Science 269.5221 (1995): 198-201.

[7] Davis, K.B., Mewes, M.O., Andrews, M.R., van Druten, N.J., Durfee, D.S., Kurn, D.M. and Ketterle, W., 1995. Bose-Einstein condensation in a gas of sodium atoms. Physical review letters, 75(22), p.3969.

[8] Kwon KA, Shipley RJ, Edirisinghe M, et al. High-speed camera characterization of voluntary eye blinking kinematics. J R Soc Interface. 2013;10(85):20130227. Published 2013 Jun 12. doi:10.1098/rsif.2013.0227

[9] Hemmerling, B., Drayna, G. K., Chae, E., Ravi, A., Doyle, J. M. (2014). Buffer gas loaded magneto-optical traps for Yb, Tm, Er and Ho. New Journal of Physics, 16(6), 063070.

[10] L. Baum, N. B. Vilas, C. Hallas, B. L. Augenbraun, S. Raval, D. Mitra, J. M. Doyle, Phys. Rev. Lett. 124, 133201 (2020).

[11] B. L. Augenbraun, Z. D. Lasner, A. Frenett, H. Sawaoka, C. Miller, T. C. Steimle, J. M. Doyle, New J. Phys 22, 022003(2020).

[12] Mitra, D., Vilas, N. B., Hallas, C., Anderegg, L., Augenbraun, B. L., Baum, L., ... Doyle, J. M. (2020). Direct Laser Cooling of a Symmetric Top Molecule. arXiv preprint

[13] L. Anderegg, L. C. Cheuk, Y. Bao, S. Burchesky, W. Ketterle, K.-K Ni, J. M. Doyle, Science 365, 1156 (2019).

[14] Foot, C. (2005). Atomic Physics. (Oxford Master Series in Physics)

[15] Griffiths, David Jeffrey, and Darrell F. Schroeter. Introduction to Quantum Mechanics. Cambridge University Press, 2019.

[16] Tiecke, T. G. (2010). Properties of potassium. University of Amsterdam, The Netherlands, Thesis, 12-14.

[17] Lindsay J. LeBlanc: Hyperfine Structure of Potassium-40, (2006).

[18] Arimondo, E., Inguscio, M., and Violino, P. (1977). Experimental determinations of the hyperfine structure in the alkali atoms. Reviews of Modern Physics, 49(1), 31.

[19] Opdam, T., Lebedev, V., and Lepoutre, S. (2012). Magneto-optical trap of 39K: setup and characterisation. Report of a, 36.

[20] Metcalf, H., Van der Straten, P. (1999). Laser cooling and trapping (Graduate texts in contemporary physics). New York: Springer.

[21] Suleymanzade, A. *Ultracold atoms experiment for trapping 39k in an optical box trap*. Doctoral dissertation, Master's thesis, University of Cambridge (2014).

[22] Tammuz, N. *Thermodynamics of ultracold ^{39}K atomic Bose gases with tuneable interactions*, ph.D. thesis, University of Cambridge (2011).

[23] Wieman, C., Flowers, G., Gilbert, S. (1995). Inexpensive laser cooling and trapping experiment for undergraduate laboratories. American Journal of Physics, 63(4), 317-330.

[24] Black, A. *Atomic cooling via AC stark shift* , Masters thesis, University of California Santa Cruz, (2014).

[25] Anderegg, L. *Ultracold molecules in optical arrays: from laser cooling to molecular collisions*, Ph.D. thesis, Harvard University (2019).

[26] Radia simulation package, The European Synchrotron.

[27] Guardado-Sanchez, E. *A Laser System for Trapping and Cooling of ^{6}Li atoms*, Bachelor of Science thesis, Massachusetts Institute of Technology.

[28] Preston, Daryl W. "Doppler-Free Saturated Absorption: Laser Spectroscopy." *American Journal of Physics*, vol. 64, no. 11, 1996, pp. 1432–1436.

[29] Becerra, E. Saturated Absorption Spectroscopy, Phys30 7LSp16 LabGuides.

[30] Pahwa K, Mudarikwa L, Goldwin J. Polarization spectroscopy and magnetically-induced dichroism of the potassium D 2 lines. Optics express. 2012 Jul 30;20(16):17456-66.

[31] Impertro, A, F. *Laser system for magneto-optical cooling and trapping of potassium* , Bachelor thesis, University of Heidelberg, (2017).

[32] *Saturated Absorption Spectroscopy*, Experiment SAS, PHY4803L Advanced Physics Laboratory Notes, University of Florida. Department of Phsyics.

[33] McCarron, D J, et al. "Modulation Transfer Spectroscopy in Atomic Rubidium." vol. 19, no. 10, 2008, p. 105601.

[34] Raj, R. K., Bloch, D., Snyder, J. J., Camy, G., and Ducloy, M. (1980). High-frequency optically heterodyned saturation spectroscopy via resonant degenerate four-wave mixing. *Physical Review Letters*, 44(19), 1251.

[35] Ekin, J. (2006). Experimental techniques for low-temperature measurements :cryostat design, material properties, and superconductor critical-current testing. Oxford: Oxford University Press.

[36] Baum, L. *Laser cooling and 1D magneto-optical trapping of calcium monohydroxide*, Ph.D. thesis, Harvard University (2020).

[37] Wilson, J. W. (1997). Shielding Strategies for Human Space Exploration: Proceedings of a Workshop Sponsored by the National Aeronautics and Space Administration and Held at Lyndon B. Johnson Space Center, Houston, Texas, December

6-8, 1995 (Vol. 3360). National Aeronautics and Space Administration, Langley Research Center.

[38] Ross, R. (2015). Quantifying MLI Thermal Conduction in Cryogenic Applications from Experimental Data. IOP Conference Series: Materials Science and Engineering. 101. 012017. 10.1088/1757-899X/101/1/012017.

[39] NRC-2 Superinsulation (2000). https://www.lakeshore.com/docs/default-source/product-downloads/installation-instructions/f069-00-00.pdf?sfvrsn=751757f94

[40] Hutzler, N. Charcoal as a Helium Cryopump: Version 1.0. 2008.

[41] Parker O-ring Handbook ORD 5700. Copyright © 2018, Parker Hannifin Corporation, Cleveland, OH.

[42] Campbell, W. *Magnetic Trapping of Imidogen Molecules*, Ph.D. thesis, Harvard University (2008).

[43] Luksch, K. *Ultracold molecules in optical arrays: from laser cooling to molecular collisions*, Thesis, National University of Singapore.

[44] Leung, A. *Characterization and optimization of laser cooling of an atomic ensemble for a quantum memory*, Bachelor of Science thesis, The Australian National University.

[45] Pyragius, T., 2012. Developing and building an absorption imaging system for Ultracold Atoms. *arXiv preprint arXiv:1209.3408.*

[46] Szulc, A. *Simulating atomic motion in a magneto-optical trap*, M.Sc Thesis, Ben-Gurion University of the Negev (2016).

This thesis was typeset using LaTeX, originally developed by Leslie Lamport and based on Donald Knuth's TeX. The body text is set in 11 point Egenolff-Berner Garamond, a revival of Claude Garamont's humanist typeface. The above illustration, *Science Experiment 02*, was created by Ben Schlitter and released under CC BY-NC-ND 3.0. A template that can be used to format a PhD dissertation with this look & feel has been released under the permissive AGPL license, and can be found online at github.com/suchow/Dissertate or from its lead author, Jordan Suchow, at suchow@post.harvard.edu.